

Computationally-driven, high throughput identification of CaTe and Li₃Sb as promising candidates for high mobility *p*-type transparent conducting materials

Viet-Anh Ha,¹ Guodong Yu,^{1,*} Francesco Ricci,¹ Diana Dahliah,¹ Michiel J. van Setten,^{1,†} Matteo Giantomassi,¹ Gian-Marco Rignanese,¹ and Geoffroy Hautier^{1,‡}

¹*Institute of Condensed Matter and Nanoscience (IMCN), Université catholique de Louvain (UCLouvain),
Chemin étoiles 8, bte L7.03.01, Louvain-la-Neuve 1348, Belgium*

(Dated: November 14, 2018)

High-performance *p*-type transparent conducting materials (TCMs) must exhibit a rare combination of properties including high mobility, transparency and *p*-type dopability. The development of high-mobility/conductivity *p*-type TCMs is necessary for many applications such as solar cells, or transparent electronic devices. Oxides have been traditionally considered as the most promising chemical space to dig out novel *p*-type TCMs. However, non-oxides might perform better than traditional *p*-type TCMs (oxides) in terms of mobility. We report on a high-throughput (HT) computational search for non-oxide *p*-type TCMs from a large dataset of more than 30,000 compounds which identified CaTe and Li₃Sb as very good candidates for high-mobility *p*-type TCMs. From our calculations, both compounds are expected to be *p*-type dopable: intrinsically for Li₃Sb while CaTe would require extrinsic doping. Using electron-phonon computations, we estimate hole mobilities at room-temperature to be about 20 and 70 cm²/Vs for CaTe and Li₃Sb, respectively. The computed hole mobility for Li₃Sb is quite exceptional and comparable with the electron mobility in the best *n*-type TCMs.

I. INTRODUCTION

Transparent conducting materials (TCMs) are necessary in many applications ranging from solar cells to transparent electronics. So far, *n*-type oxides (e.g., In₂O₃, SnO₂ and ZnO) are the highest performing TCMs, allowing them to be used in commercial devices [1–5]. On the other hand, *p*-type TCMs show poorer performances, especially in terms of carrier mobility. This hinders the development of new technologies such as transparent solar cells or transistors [3, 6]. Taking advantage of the predictive power of density functional theory (DFT) calculations, we have set up a high-throughput (HT) computational framework to identify novel *p*-type TCMs focusing first on oxide compounds [7–9].

The analysis of the calculated HT data confirmed that on average *p*-type oxides have inherently higher effective masses than *n*-type oxides [7]. This could be traced back to the strong oxygen *p*-orbital character in the valence band of most oxides and has rationalized the current gap in mobility between the best *p*-type and *n*-type oxides. This inherent difficulty in developing high-hole-mobility oxides justifies moving towards non-oxide TCM chemistries including fluorides [10], sulfides [11, 12], oxianions [13], or germanides [14]. Recently, we started extending our HT computing approach to search for non-oxide TCMs. Phosphides were identified to be among the lowest hole effective mass materials and more specifically

boron phosphide (BP) was detected as a very promising *p*-type TCM candidate [15]. We note that subsequent computational studies focusing on selected binaries and ternaries reported also on the computational screening of non-oxide TCMs [16, 17]. In the present work, we extend our HT computing approach to a larger space of chemistries and investigate some selected candidates. We screen all non-oxide compounds in a large computational data set (>34,000 semiconductors) [18]. Combining DFT-based HT computations with higher accuracy methods such as *GW*, hybrid functionals and electron-phonon coupling computations (to assess the relaxation time and thus the mobility), we identify that CaTe and Li₃Sb would be of great interest as high mobility *p*-type TCMs.

II. METHODS

All the considered materials originate from the Inorganic Crystal Structure Database (ICSD) [19]. Their relaxed crystal structures and electronic band structures were obtained from the Materials Project database [20, 21]. These rely on DFT high-throughput computations which were performed with VASP [22, 23] using the Perdew-Burke-Ernzerhof (PBE) exchange-correlation (XC) functional [24] within the projector augmented wave (PAW) framework [25].

One of the first selection criteria for TCMs is their stability. Here, it is assessed by the energy above hull E_{hull} in the Materials Project database [20]. For a compound stable at 0K, $E_{\text{hull}} = 0$ meV/atom, and the stability decreases as E_{hull} increases.

In the beginning of the screening procedure, the PBE band gap can be used as a filter. However, since PBE is known to systematically underestimate the band gap

* Present address: School of Physics and Technology (SPT), Wuhan University (WHU), Wuhan 430072, China

† Present address: IMEC, 75 Kapeldreef, B-3001 Leuven, Belgium

‡ E-mail: geoffroy.hautier@uclouvain.be

compared to experiments, more accurate calculations are needed in the subsequent steps (though with a limited number of materials). So, the fundamental and direct band gaps were also calculated with VASP for about a hundred materials using the Heyd-Scuseria-Ernzerhof (HSE) hybrid XC functional [26, 27] and adopting the same computational parameters as for the PBE calculations. For the final candidates (CaTe and Li₃Sb), G_0W_0 calculations were performed with ABINIT [28–31]. In these calculations, optimized norm-conserving (NC) pseudopotentials including semi-core electrons were used which were generated with ONCVSP [32, 33]. The kinetic cut-off energy for the wavefunctions were set to 51 and 52 Ha for CaTe and Li₃Sb respectively, as recommended in the PseudoDojo table [33]. The convergence of these calculations with respect to the kinetic energy cut-off E_c for the dielectric function and the number of bands N_b was tested using automatic GW workflows [34] based on the pymatgen [35] and AbiPy packages [31, 36]. For CaTe, the convergence of the gap at the Γ point (with a truncation error smaller than 0.01 eV) was obtained for $E_c = 12$ Ha and $N_b = 480$. In the case of Li₃Sb, the convergence is significantly faster: using $E_c = 10$ Ha and $N_b = 240$ guarantee a truncation error smaller than 0.01 eV. More details about the convergence tests are available in the supplementary document. For the calculations of the screening and the quasi-particle self-energy, $10 \times 10 \times 10$ and $8 \times 8 \times 8$ \mathbf{k} -point meshes were used for CaTe and Li₃Sb, respectively. The band structures are then interpolated from these \mathbf{k} -point meshes using AbiPy [31, 36].

The point defect computations were performed using the supercell technique [37] adopting $3 \times 3 \times 3$ supercells of the primitive cells. We calculated the defect formation energies first using the PBE XC functional but also with the more accurate HSE functional for Li₃Sb and CaTe [26, 27]. For the latter, the screening length and fraction of exact exchange were set to the common values of 0.2 Å and 25 % respectively. The kinetic energy cut-off for the wavefunctions was set to 19.1 Ha (520 eV) and the relaxations are stopped when the change in total energy between two ionic relaxation-steps is smaller than 3.67×10^{-4} Ha (0.01 eV). The formation energy of defect D in charged state q can be written as [38, 39]

$$E_f[D^q] = E[D^q] + E_{corr}[D^q] - E[bulk] - \sum_i n_i \mu_i \quad (1) \\ + q(\epsilon_{VBM} + \Delta v + \Delta \epsilon_F)$$

where $E[D^q]$ and $E[bulk]$ are the total energies of the supercell with a defect D in the charge state q and without any defects, respectively; n_i is the number of atoms of type i removed ($n_i < 0$) or added ($n_i > 0$); and, μ_i is the corresponding chemical potential. ϵ_{VBM} is the energy of the valence band maximum (VBM), and $\Delta \epsilon_F$ is the Fermi level referenced to ϵ_{VBM} . The correction terms $E_{corr}[D^q]$ and Δv are introduced to take care of the spurious image-charge interactions and the potential alignment for charged defects, respectively. The defect states with the charge q were corrected using the

extended Freysoldt’s (Kumagai’s) scheme [40, 41]. All defects computations were performed using the PyCDT package [42].

The effective masses were calculated with BoltzTrap (based on Boltzmann transport theory framework) [43] using the pymatgen [35] interface and the Fireworks workflow package [44]. All the raw effective mass data is freely available in a separate paper which covers around 48,000 inorganic materials [18]. The mobility depends on the effective mass m^* through $\mu = e\tau/m^*$ where the relaxation time τ (inverse of the scattering rate) depends on different scattering mechanisms. Carriers can be scattered by phonons, ionized and neutral impurities, grain boundaries,... In this work, we only took into account the scattering of electrons by phonons which is likely to be an important component of scattering and is an intrinsic mechanism, difficult to control through purity and microstructure. The carriers scattering by phonons can be computed theoretically if the electron-phonon matrix elements are known. In principle, one can employ Density Functional Perturbation Theory (DFPT) to obtain all the electron-phonon matrix elements from first principles. However, converging the relevant physical properties (such as the scattering rate of electrons by phonons) often requires very dense \mathbf{k} -point and \mathbf{q} -point meshes for electrons and phonons respectively leading to a considerable increase of computational time. The recently developed interpolation techniques based on Wannier functions offer a very practical and efficient solution to overcome this obstacle. In this work, we used the EPW code [45, 46] interfaced with Quantum ESPRESSO [47, 48] to calculate the relaxation-time $\tau_{n\mathbf{k}}$ (n and \mathbf{k} are band index and wave vector of a Bloch’s state, respectively). More details on the theory and the implementation can be found in Ref. 46. The $\tau_{n,\mathbf{k}}$ were interpolated on a dense $40 \times 40 \times 40$ mesh for both \mathbf{k} -points (for electrons) and \mathbf{q} -points (for phonons) starting from the DFPT values on a $6 \times 6 \times 6$ mesh. The latter (together with the structural relaxation, self-consistent, non self-consistent calculations which are needed to run EPW) were obtained using Quantum ESPRESSO with NC pseudopotentials and very stringent parameters for convergence, e.g. high cut-off energy of 40 Ha. These $\tau_{n,\mathbf{k}}$ are then used as an input to compute the carrier mobility by solving the Boltzmann transport equation by means of the BoltzTrap package [43]. In the latter calculations, the DFT band-energies (computed on a finite number of \mathbf{k} -points) are interpolated using star functions (see section 2 of Ref. 43). Here, we have implemented another interpolation for the relaxation time in BoltzTrap in order to obtain the same very dense \mathbf{k} -point grid as the one used for band-energies. The physical principle for this implementation is that the symmetries of the quasi-particle energies are the same as those of band-energies [49] ($\tau_{n,\mathbf{k}}$ due to the interaction with phonons can be calculated from the imaginary part of the electron-phonon self-energy).

III. RESULTS

Starting from the Materials Project database, our first step was to extract materials with a low hole effective mass ($< 1 m_o$, where m_o is the free electron mass) and a large enough fundamental gap (> 0.5 eV) and direct gap (> 1.5 eV), based on PBE calculations. Regarding the effective masses, in the most general form, they are represented by a tensor. As most TCMs are used as polycrystalline films, materials with isotropic or close to isotropic transport are easier to use in practical applications. Therefore, for the screening, we focus on the three principal values of this tensor and sort the materials based on the highest of the three principal hole effective masses. There were about 390 compounds passing

through this first filter.

We then screened out very unstable materials selecting only those with an energy above hull lower than 24 meV/atoms. This threshold corresponds to the typical standard deviation of computational errors (compared with experiment) of DFT formation-energies [50]. For the 107 materials passing these criteria, more accurate fundamental and direct gaps were calculated using the HSE hybrid functional. All the results of this step are presented in Table SI of the Supplemental Material [51]. For sake of clarity, Table I shows a selection of 63 materials with a direct band gap ≥ 2.8 eV. The materials are sorted in decreasing order as a function of the computed direct band gap.

TABLE I: Formula, space group, Materials Project identification number (MP-id) [20, 21], fundamental E_g and direct gaps E_g^d computed by HSE functional (in eV), energy above hull E_{hull} (in meV/atom), principal components m_1 , m_2 and m_3 of the hole effective mass tensor (in atomic units), verification of the absence of toxic/rare-earth (T/RE) elements (Be, As, Cd, Yb, Hg, Pb and Th) and of the p -type dopability (when computed here or obtained from the existing literature) for the selected compounds (see text). The materials are sorted as a function of the direct band gap in decreasing order.

Formula	Space group	MP-id	E_g^d	E_g	E_{hull}	m_1	m_2	m_3	T/RE	p -dopability
BeS	$F\bar{4}3m$	422	6.89	4.05	0.0	0.65	0.65	0.65	×	-
KMgH ₃	$Pm\bar{3}m$	23737	5.76	3.58	0.0	0.75	0.75	0.75	✓	-
SiC	$F\bar{4}3m$	8062	5.75	2.25	0.7	0.58	0.58	0.58	✓	✓ [52-55]
CsPbCl ₃	$Amm2$	675524	5.69	5.69	0.0	0.30	0.32	0.33	×	-
BeSe	$F\bar{4}3m$	1541	5.27	3.36	0.0	0.55	0.55	0.55	×	-
BeCN ₂	$I\bar{4}2d$	15703	5.21	5.21	0.0	0.75	0.75	0.78	×	-
RbPbF ₃	Cc	674508	5.20	4.84	0.0	0.71	0.83	0.95	×	-
MgS	$Fm\bar{3}m$	1315	4.95	3.84	0.0	0.98	0.98	0.98	✓	-
RbHgF ₃	$Pm\bar{3}m$	7482	4.90	2.11	0.0	0.93	0.93	0.93	×	-
AgCl	$Fm\bar{3}m$	22922	4.81	2.28	0.0	0.83	0.83	0.83	✓	-
CsHgF ₃	$Pm\bar{3}m$	561947	4.59	2.20	0.0	0.89	0.89	0.89	×	-
Be ₂ C	$Fm\bar{3}m$	1569	4.56	1.63	0.0	0.37	0.37	0.37	×	-
SrMgH ₄	$Cmc2_1$	643009	4.52	3.78	0.0	0.84	0.90	0.95	✓	-
Li ₂ Se	$Fm\bar{3}m$	2286	4.36	3.70	0.0	0.95	0.95	0.95	✓	-
BP	$F\bar{4}3m$	1479	4.35	2.26	0.0	0.34	0.34	0.34	✓	✓ [15]
CaS	$Fm\bar{3}m$	1672	4.28	3.34	0.0	0.88	0.88	0.88	✓	-
LiCa ₄ B ₃ N ₆	$Im\bar{3}m$	6799	4.25	3.38	0.0	0.86	0.86	0.86	✓	-
BaSrI ₄	$R\bar{3}m$	754852	4.22	4.22	21.8	0.73	0.73	0.80	✓	-
LiSr ₄ B ₃ N ₆	$Im\bar{3}m$	9723	4.18	3.22	0.0	0.89	0.89	0.89	✓	-
NaSr ₄ B ₃ N ₆	$Im\bar{3}m$	10811	4.08	3.14	0.0	0.92	0.92	0.92	✓	-
K ₂ LiAlH ₆	$Fm\bar{3}m$	24411	4.04	3.70	9.1	0.65	0.65	0.65	✓	-
BeTe	$F\bar{4}3m$	252	4.04	2.45	0.0	0.42	0.42	0.42	×	-
Ba ₃ SrI ₈	$I4/mmm$	756235	4.02	4.02	7.5	0.70	0.81	0.81	✓	-
CaSe	$Fm\bar{3}m$	1415	4.01	2.95	0.0	0.77	0.77	0.77	✓	-
LiH	$Fm\bar{3}m$	23703	3.97	3.97	0.0	0.46	0.46	0.46	✓	×
AlP	$F\bar{4}3m$	1550	3.90	2.50	0.0	0.56	0.56	0.56	✓	×
YbS	$Fm\bar{3}m$	1820	3.76	2.96	0.0	0.76	0.76	0.76	×	-
Na ₂ LiAlH ₆	$Fm\bar{3}m$	644092	3.75	3.75	3.9	0.66	0.66	0.66	✓	-
SrSe	$Fm\bar{3}m$	2758	3.68	3.03	0.0	0.83	0.83	0.83	✓	-
BaLiH ₃	$Pm\bar{3}m$	23818	3.62	3.26	0.0	0.36	0.36	0.36	✓	×
CsPbF ₃	$Pm\bar{3}m$	5811	3.59	3.59	4.6	0.39	0.39	0.39	×	-
Cs ₃ ZnH ₅	$I4/mcm$	643702	3.58	3.58	0.0	0.69	0.93	0.93	✓	-
Al ₂ CdS ₄	$Fd\bar{3}m$	9993	3.56	3.55	20.0	0.78	0.78	0.78	×	-
K ₂ LiAlH ₆	$R\bar{3}m$	23774	3.52	3.52	0.0	0.68	0.84	0.84	✓	-
BaMgH ₄	$Cmcm$	643718	3.51	3.26	4.8	0.48	0.55	0.70	✓	-
CaTe	$Fm\bar{3}m$	1519	3.50	2.18	0.0	0.60	0.60	0.60	✓	✓
Cs ₃ MgH ₅	$P4/ncc$	23947	3.49	3.49	0.3	0.88	0.93	0.93	✓	-
Cs ₃ MgH ₅	$I4/mcm$	643895	3.49	3.49	0.0	0.83	0.94	0.94	✓	-

Continued on next page

TABLE I – continued from previous page

Formula	Space group	MP-id	E_g^d	E_g	E_{hull}	m_1	m_2	m_3	T/RE	p -dopability
YbSe	$Fm\bar{3}m$	286	3.48	2.43	0.0	0.67	0.67	0.67	×	-
ZnS	$F\bar{4}3m$	10695	3.46	3.46	0.0	0.81	0.81	0.81	✓	✓[12]
TaCu ₃ S ₄	$P\bar{4}3m$	10748	3.46	2.95	0.0	0.98	0.98	0.98	✓	-
Al ₂ ZnS ₄	$Fd\bar{3}m$	4842	3.46	3.43	0.0	0.66	0.66	0.66	✓	×
Li ₂ ThN ₂	$P\bar{3}m1$	27487	3.46	3.33	0.0	0.85	0.95	0.95	×	-
Mg ₂ B ₂₄ C	$P\bar{4}n2$	568556	3.42	3.41	0.0	0.77	0.93	0.93	✓	-
Li ₂ GePbS ₄	$I\bar{4}2m$	19896	3.33	3.20	0.0	0.61	0.61	0.98	×	-
Cs ₃ H ₅ Pd	$P4/mbm$	643006	3.32	3.09	0.0	0.79	0.83	0.83	✓	-
SrTe	$Fm\bar{3}m$	1958	3.24	2.39	0.0	0.67	0.67	0.67	✓	×
MgTe	$F\bar{4}3m$	13033	3.24	3.24	0.9	0.95	0.95	0.95	✓	-
CsTaN ₂	$I\bar{4}2d$	34293	3.22	3.22	0.0	0.71	0.71	0.92	✓	-
Cs ₃ MnH ₅	$I4/mcm$	643706	3.21	3.18	0.0	0.82	0.96	0.96	✓	-
LiMgP	$F\bar{4}3m$	36111	3.18	2.00	0.0	0.65	0.65	0.65	✓	-
BaS	$Fm\bar{3}m$	1500	3.17	3.02	0.0	0.85	0.85	0.85	✓	-
LiAlTe ₂	$I\bar{4}2d$	4586	3.11	3.11	0.0	0.52	0.83	0.83	✓	-
YbTe	$Fm\bar{3}m$	1779	3.09	1.76	0.0	0.54	0.54	0.54	×	-
Li ₃ Sb	$Fm\bar{3}m$	2074	3.06	1.15	0.0	0.24	0.24	0.24	✓	✓
SrAl ₂ Te ₄	$I\bar{4}22$	37091	3.06	2.66	0.0	0.42	0.79	0.80	✓	-
TaCu ₃ Te ₄	$P\bar{4}3m$	9295	3.05	2.50	0.0	0.63	0.63	0.63	✓	-
TaCu ₃ Se ₄	$P\bar{4}3m$	4081	2.98	2.43	0.0	0.82	0.82	0.82	✓	-
BaSe	$Fm\bar{3}m$	1253	2.95	2.59	0.0	0.76	0.76	0.76	✓	-
KAg ₂ PS ₄	$I\bar{4}2m$	12532	2.87	2.53	0.0	0.67	0.82	0.82	✓	-
AlAs	$F\bar{4}3m$	2172	2.84	2.12	0.0	0.50	0.50	0.50	×	-
LiErS ₂	$I4_1/amd$	35591	2.80	2.80	10.4	0.62	0.99	0.99	✓	-
GaN	$F\bar{4}3m$	830	2.80	2.80	5.2	0.94	0.94	0.94	✓	-

Among the materials at the top of the list, SiC is a well-known wide band gap semiconductor. This material exhibits polymorphism (e.g. cubic: 3C, Rhombohedral: 15R, hexagonal: 6H, 4H, 2H) [56] and can be doped both n - and p -type [52–55]. A high hole mobility of 40 cm²/Vs was obtained for the cubic phase [57]. The indirect optical absorption of cubic phase is very weak at room temperature with a coefficient of 10³ cm⁻¹ at 3.1 eV [58]. We suggest that SiC can be considered as a good p -type TCM. The main disadvantage of this compound is the difficulty of hole doping. Most known impurities such as Al, B, Ga and Sc create deep doping-levels leading to rather low concentrations of holes which were typically measured to be lower than 10¹⁸ cm⁻³ [57] and is suitable for transistor applications.

Next comes a series of beryllium based compounds (BeS, BeSe, BeCN₂, Be₂C and BeTe). While their computed performance in terms of band gap and hole effective masses are very attractive, the toxicity of beryllium lowers their interest for technological applications. Likewise, the many lead-based halide perovskites (CsPbCl₃, RbPbF₃, and CsPbF₃) and Li₂GePbS₄ also present toxicity issues. It is interesting however to see these halide perovskites being of great interest as solar absorbers when they are made in chemistries showing smaller gaps [59, 60]. Toxicity is also an issue with the series of arsenides, e.g. AlAs. These arsenides are also very analogous to the phosphides such as BP and AlP that were identified in a previous work [15]. Some of the materials in the list contain rare-earth elements which might

present some cost issues. We consider that further assessment of all these materials in terms of dopability and mobility is not a priority. Therefore, in the penultimate column of Table I, the absence of toxic or rare-earth elements is verified, as indicated by a checkmark.

Continuing to explore the list of materials, many hydrides appear to be of interest with low hole effective mass and large direct band gaps for LiH, BaLiH₃ and CsH. Unfortunately, our subsequent defect computations indicate that these hydrides have low-lying hole-killing defects especially the hydrogen vacancy making unlikely their efficient p -type doping (see the Supplemental Material [51]). A few sulfides are also identified by our screening: ZnS and ZnAl₂S₄. ZnS has been indeed recently studied as a good performance p -type TCM [12]. ZnAl₂S₄, on the other hand, is less studied but our defect computation indicates that it is very unlikely to be p -type dopable because Zn-Al anti-site defects form easily and act as hole-killers. Al₂CdS₄ is likely to present the same issues. The defect formation energies computed by DFT for ZnAl₂S₄ are given in the Supplemental Material [51].

Among the different materials in the table, two promising candidates, Li₃Sb and CaTe, also attracted our attention. The rest of the paper is dedicated to the further computations that were performed for these compounds.

The conventional cells of CaTe and Li₃Sb are shown in Fig. 1 (a) and (e). Ca atoms in CaTe are surrounded by six Te atoms forming an octahedral local environment. In Li₃Sb, the cation fills tetrahedral and octahedral sites. Both CaTe and Li₃Sb are cubic phases with high symmetry, which explains for their isotropy in hole effective

masses ($m_1 = m_2 = m_3$). CaTe and Li₃Sb exhibit very low hole effective masses with the eigenvalues being 0.60 and 0.25 m_o (m_o -mass of free electron), respectively. It is worth noting that the lowest hole effective masses found so far in a computational database for a p -type conducting oxides K₂Sn₂O₃ [7, 61] is 0.27 m_o . The promising non-oxide p -type TCM reported recently [15], BP, shows an effective mass around 0.35 m_o . Current Cu-based p -type TCOs show effective masses around 1.5 to 2 m_o [7]. The direct gaps of CaTe and Li₃Sb calculated using HSE hybrid functional are 3.5 and 3.06 eV respectively. Next to hybrid functional computations, we performed G_0W_0 to confirm the value of these band gaps.

Fig. 1 (b) shows DFT band structure with a scissor shift to fit G_0W_0 fundamental gap (G_0W_0 band structure of CaTe is shown in Fig. S6 of the Supplemental Material [51]). The G_0W_0 fundamental gap ($\Gamma - X$) is 2.95 eV while the direct gap is located at X -point and has a value of 4.14 eV. The G_0W_0 direct gap is consistent with the optical gap of 4.1 eV measured experimentally [62]. We expect such a large band gap to lead to transparency in the visible region. Li₃Sb is also an indirect semiconductor. In the same way, the DFT electronic band structure with a scissor shift is presented in Fig. 1 (f) (see Fig. S7 of the Supplemental Material [51] for G_0W_0 band structure). The G_0W_0 band gap and direct gap are 1.37 and 3.17 eV, respectively. The G_0W_0 direct gap (located at the Γ -point) of 3.17 eV. This is consistent with a experimental value of 3.1 eV measured recently [63] but much lower than another experimental value of 3.9 eV reported earlier [64]. The indirect band gap is narrow and will lead to some absorption in the visible range. However, the indirect nature of the absorption makes it phonon-assisted and is expected to lead to weak absorption. To quantify this absorption, we computed the optical absorption including phonon-assisted processes using EPW [45, 46]. Details about computational method can be found in Ref. 65. The result in Fig. 2 shows quite weak absorption in the visible range with the average intensity about $5 \times 10^3 \text{ cm}^{-1}$, which means that a 100-nm film still allows more than 70 % of visible light energy to get through. This is suitable for applications and devices using thin-film form of Li₃Sb. The weak indirect optical absorption computed here is similar to that of established p -type TCOs such as SnO [66] or recently proposed p -type TCMs such as BP [15].

CaTe and Li₃Sb show very low hole effective mass (0.60 and 0.24 m_o within DFT). Indeed, both materials have threefold degeneracy at VBM (Γ point), therefore, the transport of holes occurs in three bands with some lighter and some heavier. Our definition of effective mass takes into account the competition among these three bands and give an average value that is representative of the transport which will happen in the different bands. More details about formulas and calculation techniques can be found in Ref. [18, 67]. This should be kept in mind when comparing our results to other studies which sometimes only focus on one band when several competing bands are

present [16, 68]. Fig. 1 shows projected density of states (DOS) for (c) CaTe and (g) Li₃Sb. For both compounds, the top of valence band is mainly of anionic p -orbital characters (Sb³⁻ or Te²⁻) with some mixing from the cations. The effective masses are directly related to overlap and energy difference between orbitals [67]. The lower value of hole effective masses obtained in these non-oxide compounds can be associated to both a better alignment between the anionic and cationic states than in oxides and larger anionic p -orbitals (5 p and 4 p versus 2 p for oxides).

The effective mass is an important factor driving carrier mobility but not the only one. Scattering rate or relaxation time also affects the mobility. There are several mechanisms which can influence relaxation time as mentioned in II. Phonon scattering is the most intrinsic factor as it is not affected by purity and microstructure. The evaluation of relaxation time from phonon scattering can be performed *ab initio* using electron-phonon coupling matrices obtained from DFPT phonon computations. Fig. 3 shows phonon band structures (fat bands) and projected DOS of phonons for (a) CaTe and (b) Li₃Sb. The fat bands represent qualitatively characteristics of vibrational modes including what type of atoms participates in the phonon modes at a given energy, their direction and amplitude. The absence of modes with negative (purely imaginary) frequencies show that these materials are dynamically stable at 0 K. The lighter atoms (Ca and Li) mainly contribute to the optical modes at high frequencies (3 and 9 modes in CaTe and Li₃Sb, respectively) while the heavier elements (Te and Sb) play an important role in the three acoustic modes at low frequencies.

Using the DFPT phonon computations and EPW, we can extract electron-phonon coupling matrices and the relaxation time $\tau_{n\mathbf{k}}$ on a dense \mathbf{k} -point grid (see Eq. S1 of the Supplemental Material [51]). Fig. 1 (d) and (h) show the scattering rate and lifetime (inverse of scattering rate) as a function of energy at 300 K for CaTe and Li₃Sb respectively (see Eq. S2 of the Supplemental Material [51]). As commonly observed, the scattering rate is proportional to the DOS. A higher DOS offer more states available for the scattered electrons. At the doping hole concentration of 10^{18} cm^{-3} , the Fermi levels are 90.5 and 120.8 meV above the VBMs for CaTe and Li₃Sb, respectively. For the highest doping of 10^{21} cm^{-3} , the Fermi levels lie below VBMs of 264.5 and 168.5 meV for CaTe and Li₃Sb, respectively. The transport of holes, therefore, takes place around VBMs (Γ -points). The DOS at Γ -point of Li₃Sb is larger than that of CaTe but the scattering rate of Li₃Sb are fairly similar (see Fig. 1 (d) and (h)) indicating that a slightly weaker electron-phonon coupling is present in Li₃Sb.

We computed scattering rates at temperatures of 300 and 400 K. Fig. 4 shows the hole mobilities as a function of hole concentrations at 300 and 400 K for both CaTe and Li₃Sb. The mobilities decreases with hole concentrations. As the Fermi levels shifts deeper below the

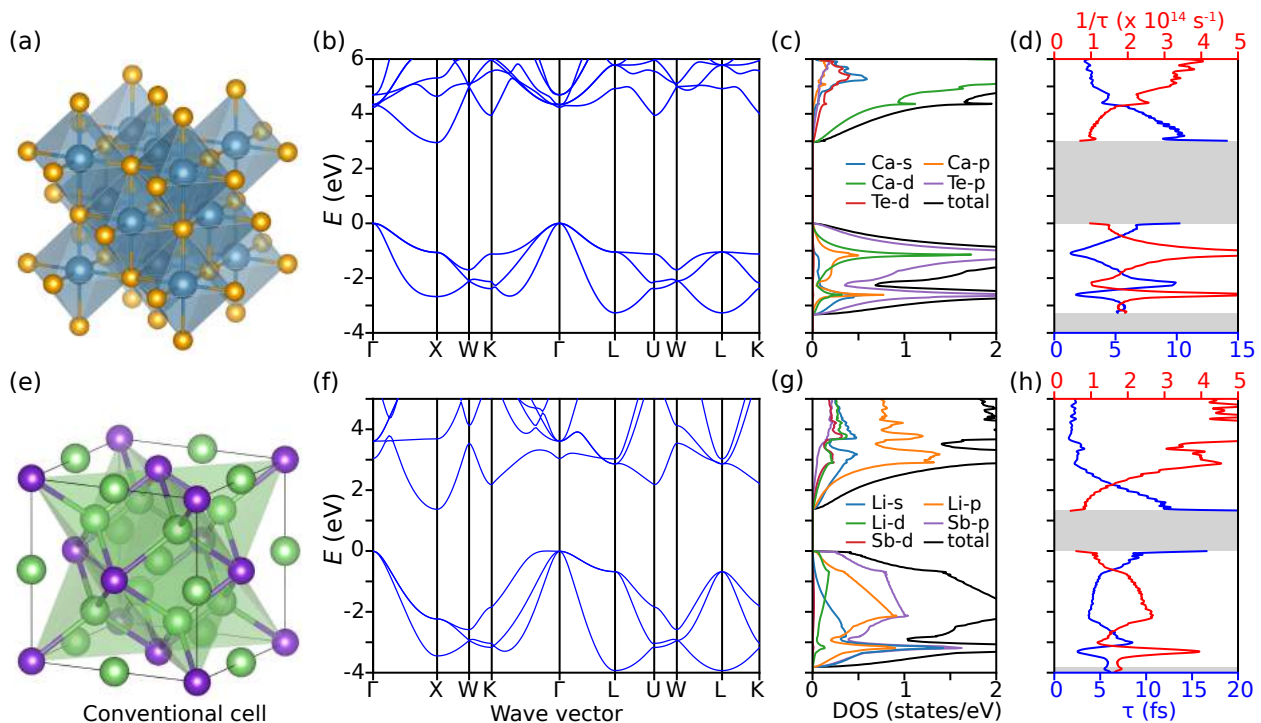


FIG. 1. From the left to the right, the conventional cells, band structures, projected density of states (DOS) and relaxation time and scattering rate. Sub-figures (a)-(d) and (e)-(h) show data of CaTe and Li₃Sb respectively. The conventional cells present local environments around cations Ca (blue) and Li (green). (b) and (f) plot DFT band structures with a rigid shift of the conduction bands (scissor operator) to fit the fundamental gaps computed by G_0W_0 . (d) and (h) show relaxation time τ (in femto-second) and scattering rate $1/\tau$ (in 1/second) as functions of energy at temperature 300 K. The projected DOS in (c) and (g) are computed by DFT. The band gaps of DOS and relaxation time are also shifted to fit G_0W_0 values.

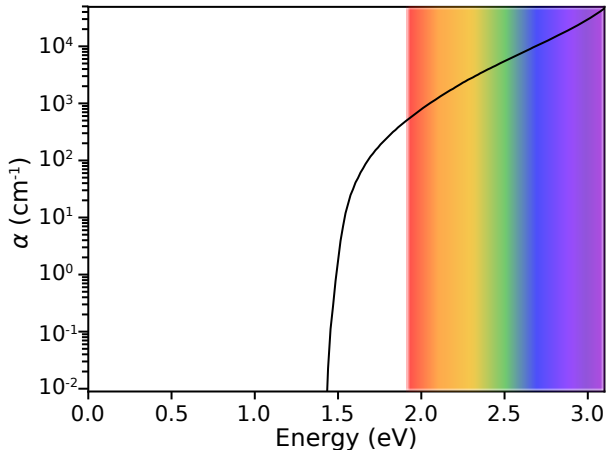


FIG. 2. The indirect optical absorption of Li₃Sb due to phonon-assisted transitions.

VBM, the DOS increases as well as the scattering rate (see Fig. 1 (d) and (h)). CaTe shows values of hole mobility around 20 cm²/Vs that is comparable with the mobility of Ba₂BiTaO₆, a recently reported *p*-type TCO [9], and larger than mobilities of the traditional *p*-type TCOs such as CuAlO₂ [69] and SnO [70]. Li₃Sb exhibits an exceptional hole mobility up to about 70 cm²/Vs at room-temperature. This value nearly reaches the val-

ues of the electron mobilities of the best current *n*-TCOs such as SnO₂, ZnO, In₂O₃ and Ga₂O₃ which are around 100 cm²/Vs (see Table SII of the Supplemental Material [51]). It is worth noting that the mobility measured experimentally take into account other scattering processes. Our computed mobilities as they only take into account phonon scattering can be seen as an upper bound.

Our final assessment focuses on the dopability of CaTe and Li₃Sb. While we have assumed so far that the Fermi level of these two materials could be tuned to generate hole carriers, it remains to be seen if the defect chemistry is favorable to hole generation. To answer this question, we performed defect calculations using a HSE following the procedure described in section II. Fig. 5 (a) presents the defect formation energy for both intrinsic and extrinsic defects for each sort of defect in CaTe. The chemical potentials are chosen in conditions which lead to the most favorable *p*-type doping tendency for this material. The chemical potentials corresponding to different conditions in the phase diagrams are available in Fig. S8 of the Supplemental Material [51]. Focusing first on intrinsic defects only including vacancies, anti-site defects and interstitial atoms, defect formation energies of these are plotted in Fig. 5 (a) with chemical potentials extracted in Te-rich condition of the phase diagram. Intrinsically, CaTe is unlikely to present *p*-type doping as no intrinsic

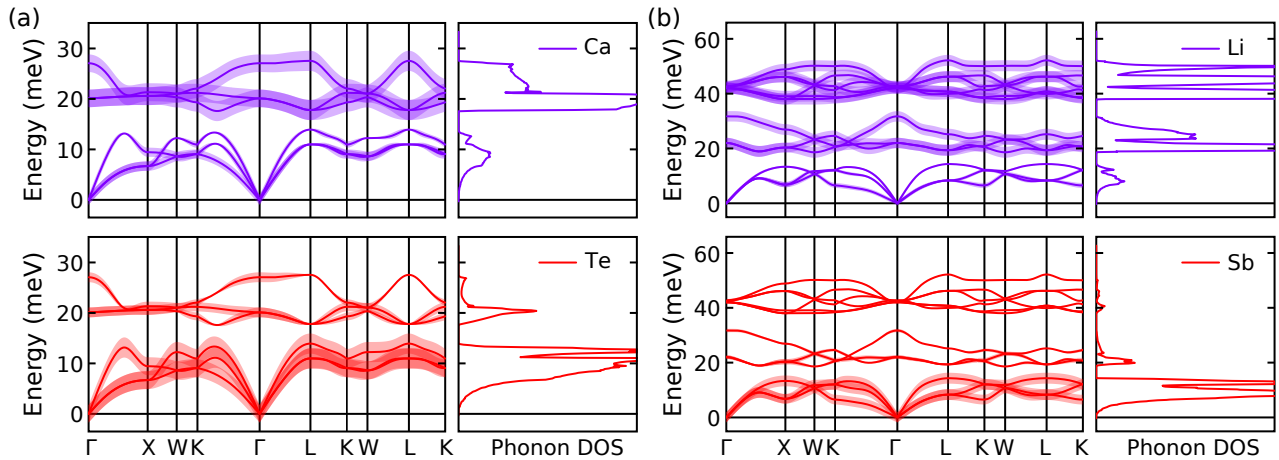


FIG. 3. Phonon band structures with fat bands representing displacements of atomic vibrations. The width of fat bands gives qualitative understanding of the vibrational modes such as what are the atomic types involved in the vibrations at a given energy, their direction of oscillation and the amplitude (related to the displacement). The projected DOS of phonons on each type of atom are correspondingly shown next to the band structures. (a) CaTe and (b) Li_3Sb .

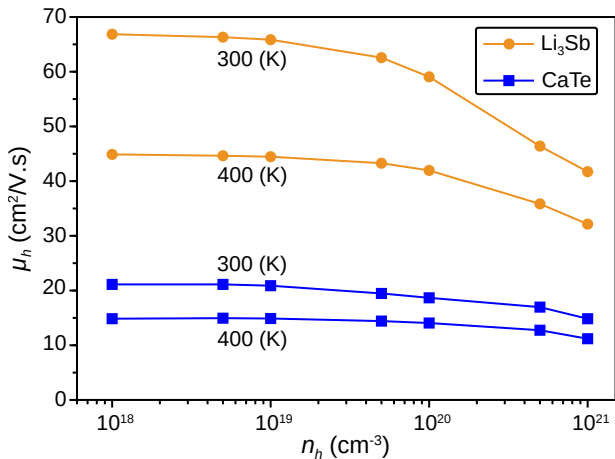


FIG. 4. Hole mobilities as a function of hole concentrations of CaTe and Li_3Sb at temperatures 300 and 400 K.

defect acts as a low lying acceptor. The vacancy of Ca will be in competition with the hole killing vacancy of Te leading to a fermi level far from the valence band. However, the Te vacancy is not low enough in energy that it would prevent extrinsic p -type doping. When extrinsic defects with Na, K and Li substituting onto Ca-sites are considered, we find that all these substitutions offer shallow acceptor very competitive compared to the Te vacancy. The Ca by Na substitution is the lowest in energy. Extrinsic doping by Na might therefore lead to p -type doping in CaTe. The plots of formation energies of K_{Ca} , Na_{Ca} and Li_{Ca} in Fig. 5 (a) were achieved with chemical potentials extracted from $\text{KTe}-\text{CaTe}-\text{K}_2\text{Te}_3$, $\text{NaTe}_3-\text{CaTe}-\text{Na}_2\text{Te}$ and $\text{Li}_2\text{Te}-\text{CaTe}-\text{Te}$ facets of the three-element phase diagrams (see Fig. S8 of the Supplemental Material [51]). For Li_3Sb , Fig. 5 (b) shows an intrinsic tendency for hole doping with the lithium vacancy (Va_{Li}) acting as a shallow acceptor with a very

low formation energy and no competing hole-killer. This plot is produced with chemical potentials computed in $\text{Li}_3\text{Sb}-\text{Li}_2\text{Sb}$ facet of the phase diagram (see Fig. S9 of the Supplemental Material [51]).

IV. DISCUSSIONS

The discovery of the quite unanticipated Li_3Sb with a potential for very high hole mobility demonstrates the interest of our HT screening strategy. Li_3Sb is an unexpected compound for TCM applications and would have been difficult to intuitively identify. Among other A_3B compounds ($\text{A} = \text{Li}, \text{Na}, \text{K}$ and Rb ; and $\text{B} = \text{N}, \text{P}, \text{As}$ and Sb), Li_3Sb is exceptional because of its very low hole effective masses (see Table SIII in the Supplemental Material [51]). We suggest that the energy difference between $\text{A-}ns^1$ ($n = 2, 3, 4, 5$ for $\text{Li}, \text{Na}, \text{K}$ and Rb , respectively) and $\text{B-}np^3$ ($n = 2, 3, 4, 5$ for $\text{N}, \text{P}, \text{As}$ and Sb , respectively) orbitals of valence electrons (A and B) might play important role here. In fact, the energy difference between $\text{Li-}2s^1$ and $\text{Sb-}5p^3$ is about 1.954 (eV) [33] and is the smallest value among many other ones of $\text{A-}ns^1/\text{B-}np^3$ pairs. This leads to a small orbital-energy difference and strong s/p (anti-)bonding, which results in low hole effective mass. While we only focus on CaTe and Li_3Sb as they are likely the most potential candidates, there are other interesting materials with hole effective masses from 0.6 to 1.0 m_o and high direct gaps (see Table I) such as CaS, SrSe, SrTe, $\text{LiCa}_4\text{B}_3\text{N}_6$, $\text{LiSr}_4\text{B}_3\text{N}_6$, $\text{NaSr}_4\text{B}_3\text{N}_6$... Defects calculations for these materials have not performed in this work and we, therefore, cannot adjudge their p -type doping-tendency.

By going beyond oxides, we identified compounds with very high hole mobility. However, several other issues also arise and need to be considered. The processing of antimonides or tellurides might be more difficult than

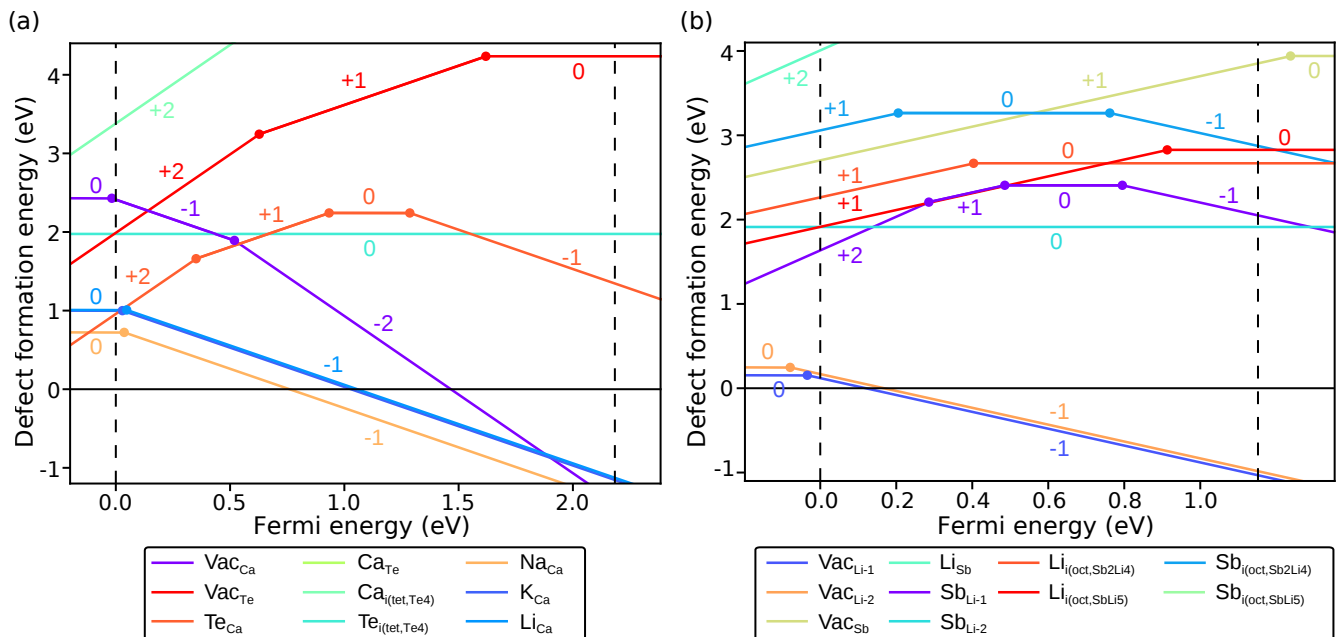


FIG. 5. The defect formation energy as a function of Fermi level of intrinsic and extrinsic defects for (a) CaTe and (b) Li_3Sb . For CaTe, the intrinsic defects include vacancies (Vac_{Ca} and Vac_{Te}), anti-sites (Te_{Ca} and Ca_{Te}) and interstitial atoms inserted into the tetrahedral hollows formed by 4 Te atoms ($\text{Ca}_{\text{i}(\text{tet},\text{Te}4)}$ and $\text{Te}_{\text{i}(\text{tet},\text{Te}4)}$) while Na, K and Li are used as the extrinsic defects substituting Ca atoms (Na_{Ca} , K_{Ca} and Li_{Ca}). For Li_3Sb , the intrinsic defects include vacancies ($\text{Vac}_{\text{Li}-1}$, $\text{Vac}_{\text{Li}-2}$ and Vac_{Sb}), anti-sites (Li_{Sb} , $\text{Sb}_{\text{Li}-1}$ and $\text{Sb}_{\text{Li}-2}$) and interstitial atoms inserted into the octahedral hollows formed by Sb and Li atoms ($\text{Li}_{\text{i}(\text{oct},\text{Sb}2\text{Li}4)}$, $\text{Li}_{\text{i}(\text{oct},\text{SbLi}5)}$, $\text{Sb}_{\text{i}(\text{oct},\text{Sb}2\text{Li}4)}$ and $\text{Sb}_{\text{i}(\text{oct},\text{SbLi}5)}$). In both cases, the VBM is set to zero.

oxides. They are, however, very common chemistries in other applications such as thermoelectrics with several exemplary compounds such as PbTe , Bi_2Te_3 [71], or more recently Mg_3Sb_2 [72–74]. The band gaps in non-oxide compounds are narrower, which lowers in average their transparency in the visible light. As we already discussed [15], this can be overcome by exploiting the indirect gaps and weak phonon-assisted optical transitions. Lower band gaps are useful for p -dopability though as lower band gap materials tend to be easier to dope [75].

We note that the defect chemistry of non-oxide can be different than in traditional TCOs. For oxides, the cation-anion anti-site defects (replacement of anions on cations' sites and vice versa) are unlikely to be favorable energetically because of the large electronegativity difference between cations and anions. In non-oxide compounds, *e.g.* CaTe, the cation-anion anti-sites are more likely to be present leading to potentially different hole-killing defects. While the anion (oxygen) vacancy is the most common hole-killer in oxides, we see our non-oxide materials presenting anti-sites cation-anion defects lower in energy than the anion vacancy such as in CaTe. We also identify that the hydride chemistry while offering attractive electronic structures presents dopability issues (*i.e.*, a low lying hydrogen vacancy acting as hole killer) preventing them for further consideration in p -type TCMs.

V. CONCLUSIONS

Using a large database and appropriate filtering strategies, we report on a high-throughput search for non-oxide p -type TCMs. We identified two materials to be of interest: CaTe and Li_3Sb . We performed extensive follow-up computational investigation of these candidates, evaluating their band structure using beyond DFT techniques, their transport and phonon-assisted optical properties using electron-phonon computations as well as their defect chemistry. Both CaTe and Li_3Sb present very attractive properties for p -type TCM applications. The Li_3Sb shows a very high hole mobility of around $70 \text{ cm}^2/\text{Vs}$, which is close to electron mobility in the best n -type TCMs. Our work motivates further experimental investigation of these two materials for TCM applications.

VI. ACKNOWLEDGMENTS

V.-A.H. was funded through a grant from the FRIA. G.-M.R. is grateful to the F.R.S.-FNRS for financial support. G.H., G.-M.R., G.Y. and F.R. acknowledge the F.R.S.-FNRS project HTBaSE (contract N° PDR-T.1071.15) for financial support. We acknowledge access to various computational resources: the Tier-1 supercomputer of the Fédération Wallonie-Bruxelles funded by the Walloon Region (grant agreement N° 1117545), and all the facilities provided by the Université catholique de

Louvain (CISM/UCLouvain) and by the Consortium des Équipements de Calcul Intensif en Fédération Wallonie

Bruxelles (CÉCI). The authors thank Dr. Samuel Poncé and Professor Emmanouil Kioupakis for helpful discussions on the technical aspects of the electron-phonon computations.

-
- [1] H. Ohta and H. Hosono, *Mater. Today* **7**, 42 (2004).
- [2] A. Facchetti and T. J. Marks, eds., “Transparent electronics: From synthesis to applications,” (Wiley, 2010).
- [3] K. Ellmer, *Nat. Photonics* **6**, 809 (2012).
- [4] P. Barquinha, R. Martins, L. Pereira, and E. Fortunato, “Transparent oxide electronics: From materials to devices,” (Wiley, 2012).
- [5] E. Fortunato, P. Barquinha, and R. Martins, *Adv. Mater.* **24**, 2945 (2012).
- [6] S. C. Dixon, D. O. Scanlon, C. J. Carmalt, and I. P. Parkin, *J. Mater. Chem. C* **4**, 6946 (2016).
- [7] G. Hautier, A. Miglio, G. Ceder, G.-M. Rignanese, and X. Gonze, *Nat. Commun.* **4**, 2292 (2013).
- [8] J. B. Varley, V. Lordi, A. Miglio, and G. Hautier, *Phys. Rev. B* **90**, 045205 (2014).
- [9] A. Bhatia, G. Hautier, T. Nilgianskul, A. Miglio, J. Sun, H. J. Kim, K. H. Kim, S. Chen, G.-M. Rignanese, X. Gonze, and J. Suntivich, *Chem. Mater.* **28**, 30 (2016).
- [10] H. Yanagi, J. Tate, S. Park, C.-H. Park, and D. Keszler, *Appl. Phys. Lett.* **82**, 2814 (2003).
- [11] S. Park, D. A. Keszler, M. M. Valencia, R. L. Hoffman, J. P. Bender, and J. F. Wager, *Appl. Phys. Lett.* **80**, 4393 (2002).
- [12] R. Woods-Robinson, J. K. Cooper, X. Xu, L. T. Schelhas, V. L. Pool, A. Faghaninia, C. S. Lo, M. F. Toney, I. D. Sharp, and J. W. Ager, *Adv. Electron. Mater.* **2**, 1500396 (2016).
- [13] K. Ueda, S. Inoue, S. Hirose, H. Kawazoe, and H. Hosono, *Appl. Phys. Lett.* **77**, 2701 (2000).
- [14] F. Yan, X. Zhang, Y. G. Yu, L. Yu, A. Nagaraja, T. O. Mason, and A. Zunger, *Nat. Commun.* **6**, 7308 (2015).
- [15] J. B. Varley, A. Miglio, V.-A. Ha, M. J. van Setten, G.-M. Rignanese, and G. Hautier, *Chem. Mater.* **29**, 2568 (2017).
- [16] R. K. M. Raghupathy, T. D. Kühne, C. Felser, and H. Mirhosseini, *J. Mater. Chem. C* **6**, 541 (2018).
- [17] R. K. M. Raghupathy, H. Wiebeler, T. D. Kühne, C. Felser, and H. Mirhosseini, *Chem. Mater.* (2018), 10.1021/acs.chemmater.8b02719.
- [18] F. Ricci, W. Chen, U. Aydemir, G. J. rey Snyder, G.-M. Rignanese, A. Jain, and G. Hautier, *Sci. Data* **4**, 170085 (2017).
- [19] “Inorganic Crystal Structure Database,” <https://www.fiz-karlsruhe.de/de/leistungen/kristallographie/icsd.html> (2013), [FIZ Karlsruhe: Karlsruhe, Germany, 2013].
- [20] A. Jain, S. P. Ong, G. Hautier, W. Chen, W. D. Richards, S. Dacek, S. Cholia, D. Gunter, D. Skinner, G. Ceder, and K. A. Persson, *APL Materials* **1**, 011002 (2013).
- [21] “The Materials Project,” <https://www.materialsproject.org/> (2013), [accessed September 1, 2013].
- [22] G. Kresse and J. Furthmüller, *Comput. Mater. Sci.* **6**, 15 (1996).
- [23] G. Kresse and J. Furthmüller, *Phys. Rev. B* **54**, 11169 (1996).
- [24] J. Perdew, K. Burke, and M. Ernzerhof, *Phys. Rev. Lett.* **77**, 3865 (1996).
- [25] P. E. Blöchl, *Phys. Rev. B* **50**, 17953 (1994).
- [26] J. Heyd, G. E. Scuseria, and M. Ernzerhof, *J. Chem. Phys.* **118**, 8207 (2003).
- [27] E. N. Brothers, A. F. Izmaylov, J. O. Normand, V. Barone, and G. E. Scuseria, *J. Chem. Phys.* **129**, 011102 (2008).
- [28] X. Gonze, J.-M. Beuken, R. Caracas, F. Detraux, M. Fuchs, G.-M. Rignanese, L. Sindic, M. Verstraete, G. Zerah, F. Jollet, M. Torrent, A. Roy, M. Mikami, P. Ghosez, J.-Y. Raty, and D. C. Allan, *Comput. Mater. Sci.* **25**, 478 (2002).
- [29] X. Gonze, *Z. Kristallogr.* **202**, 558 (2005).
- [30] X. Gonze, B. Amadon, P.-M. Anglade, J.-M. Beuken, F. Bottin, P. Boulanger, F. Bruneval, D. Caliste, R. Caracas, M. Côté, T. Deutsch, L. Genovese, P. Ghosez, M. Giantomassi, S. Goedecker, D. R. Hamann, P. Hermet, F. Jollet, G. Jomard, S. Leroux, M. Mancini, S. Mazevet, M. J. T. Oliveira, G. Onida, Y. Pouillon, T. Rangel, G.-M. Rignanese, D. Sangalli, R. Shaltaf, M. Torrent, M. J. Verstraete, G. Zerah, and J. W. Zwanziger, *Comput. Phys. Commun.* **180**, 2582 (2009).
- [31] X. Gonze, F. Jollet, F. A. Araujo, D. Adams, B. Amadon, T. Applencourt, C. Audouze, J.-M. Beuken, J. Bieder, A. Bokhanchuk, E. Bousquet, F. Bruneval, D. Caliste, M. Côté, F. Dahm, F. D. Pieve, M. Delaveau, M. D. Gennaro, B. Dorado, C. Espejo, G. Geneste, L. Genovese, A. Gerossier, M. Giantomassi, Y. Gillet, D. R. Hamann, L. He, G. Jomard, J. L. Janssen, S. L. Roux, A. Levitt, A. Lherbier, F. Liu, I. Lukačević, A. Martin, C. Martins, M. J. T. Oliveira, S. Poncé, Y. Pouillon, T. Rangel, G.-M. Rignanese, A. H. Romero, B. Rousseau, O. Rubel, A. A. Shukri, M. Stankovski, M. Torrent, M. J. V. Setten, B. V. Troeye, M. J. Verstraete, D. Waroquiers, J. Wiktor, B. Xu, A. Zhou, and J. W. Zwanziger, *Comput. Phys. Commun.* **205**, 106 (2016).
- [32] D. R. Hamann, *Phys. Rev. B* **88**, 085117 (2013).
- [33] M. J. van Setten, M. Giantomassi, E. Bousquet, M. J. Verstraete, D. R. Hamann, X. Gonze, and G.-M. Rignanese, *Comput. Phys. Commun.* **226**, 39 (2018).
- [34] M. J. van Setten, M. Giantomassi, X. Gonze, G.-M. Rignanese, and G. Hautier, *Phys. Rev. B* **96**, 155207 (2017).
- [35] S. P. Ong, W. D. Richards, A. Jain, G. Hautier, M. Kocher, S. Cholia, D. Gunter, V. L. Chevrier, K. A. Persson, and G. Ceder, *Comput. Mater. Sci.* **68**, 314 (2013).
- [36] M. Giantomassi *et al.*, “Open-source library for analyzing the results produced by ABINIT,” <https://github.com/abinit/abipy> (2014).
- [37] C. Freysoldt, B. Grabowski, T. Hickel, J. Neugebauer, G. Kresse, A. Janotti, and C. G. Van de Walle, *Rev. Mod. Phys.* **86**, 253 (2014).

- [38] H.-P. Komsa, T. T. Rantala, and A. Pasquarello, *Phys. Rev. B* **86**, 045112 (2012).
- [39] S. B. Zhang and J. E. Northrup, *Phys. Rev. Lett.* **67**, 2339 (1991).
- [40] C. Freysoldt, J. Neugebauer, and C. G. Van de Walle, *Phys. Status Solidi B* **248**, 1067 (2011).
- [41] Y. Kumagai and F. Oba, *Phys. Rev. B* **89**, 195205 (2014).
- [42] D. Broberg, B. Medasani, N. E. Zimmermann, G. Yu, A. Canning, M. Haranczyk, M. Asta, and G. Hautier, *Comput. Phys. Commun.* **226**, 165 (2018).
- [43] G. K. H. Madsen and D. J. Singh, *Comput. Phys. Commun.* **175**, 67 (2006).
- [44] A. Jain, S. P. Ong, W. Chen, B. Medasani, X. Qu, M. Kocher, M. Brafman, G. Petretto, G.-M. Rignanese, G. Hautier, D. Gunter, and K. A. Persson, *Concurr. Comput. Pract. Exp.* **27**, 5037 (2015).
- [45] J. Noffsinger, F. Giustino, B. D. Malone, C.-H. Park, S. G. Louie, and M. L. Cohen, *Comput. Phys. Commun.* **181**, 2140 (2010).
- [46] S. Ponc e, E. R. Margine, C. Verdi, and F. Giustino, *Comput. Phys. Commun.* **209**, 116 (2016).
- [47] P. Giannozzi, S. Baroni, N. Bonini, M. Calandra, R. Car, C. Cavazzoni, D. Ceresoli, G. L. Chiarotti, M. Cococcioni, I. Dabo, A. Dal Corso, S. de Gironcoli, S. Fabris, G. Fratesi, R. Gebauer, U. Gerstmann, C. Gougoussis, A. Kokalj, M. Lazzeri, L. Martin-Samos, N. Marzari, F. Mauri, R. Mazzarello, S. Paolini, A. Pasquarello, L. Paulatto, C. Sbraccia, S. Scandolo, G. Sclauzero, A. P. Seitsonen, A. Smogunov, P. Umari, and R. M. Wentzcovitch, *J. Phys.: Condens. Matter* **21**, 395502 (2009).
- [48] P. Giannozzi, O. Andreussi, T. Brumme, O. Bunau, M. Buongiorno Nardelli, M. Calandra, R. Car, C. Cavazzoni, D. Ceresoli, M. Cococcioni, N. Colonna, I. Carnimeo, A. Dal Corso, S. de Gironcoli, P. Delugas, R. A. DiStasio, A. Ferretti, A. Floris, G. Fratesi, G. Fugallo, R. Gebauer, U. Gerstmann, F. Giustino, T. Gorni, J. Jia, M. Kawamura, H.-Y. Ko, A. Kokalj, E. K uc ukbenli, M. Lazzeri, M. Marsili, N. Marzari, F. Mauri, N. L. Nguyen, H.-V. Nguyen, A. O. de-la Roza, L. Paulatto, S. Ponc e, D. Rocca, R. Sabatini, B. Santra, M. Schlipf, A. P. Seitsonen, A. Smogunov, I. Timrov, T. Thonhauser, P. Umari, N. Vast, X. Wu, and S. Baroni, *J. Phys.: Condens. Matter* **29**, 465901 (2017).
- [49] M. Giantomassi, *Core-electrons and self-consistency in the GW approximation from a PAW perspective*, Ph.D. thesis, Universit e catholique de Louvain (2009), chapter 5 and appendix B.
- [50] G. Hautier, S. P. Ong, A. Jain, C. J. Moore, and G. Ceder, *Phys. Rev. B* **85** (2012), 10.1103/physrevb.85.155208.
- [51] See See Supplemental Material at [URL will be inserted by publisher].
- [52] K. Furukawa, A. Uemoto, M. Shigeta, A. Suzuki, and S. Nakajima, *Appl. Phys. Lett.* **48**, 1536 (1986).
- [53] Y. Kondo, T. Takahashi, K. Ishii, Y. Hayashi, E. Sakuma, S. Misawa, H. Daimon, M. Yamanaka, and S. Yoshida, *IEEE Electron Device Lett.* **7**, 404 (1986).
- [54] K. Shibahara, N. Kuroda, S. Nishino, and H. Matsunami, *Jpn. J. Appl. Phys.* **26**, 1815 (1987).
- [55] R. Weing artner, P. J. Wellmann, M. Bickermann, D. Hofmann, T. L. Straubinger, and A. Winnacker, *Appl. Phys. Lett.* **80**, 70 (2002).
- [56] W. J. Choyke and G. Pensl, *MRS Bull.* **22**, 25 (1997).
- [57] H. Morko c, S. Strite, G. B. Gao, M. E. Lin, B. Sverdlov, and M. Burns, *J. Appl. Phys.* **76**, 1363 (1994).
- [58] H. R. Philipp, *Phys. Rev.* **111**, 440 (1958).
- [59] M. Liu, M. B. Johnston, and H. J. Snaith, *Nature* **501**, 395 (2013).
- [60] M. A. Green, A. Ho-Baillie, and H. J. Snaith, *Nat. Photonics* **8**, 506 (2014).
- [61] V.-A. Ha, F. Ricci, G.-M. Rignanese, and G. Hautier, *J. Mater. Chem. C* **5**, 5772 (2017).
- [62] G. A. Saum and E. B. Hensley, *Phys. Rev.* **7**, 1019 (1959).
- [63] T. J. Richardson, *Solid State Ionics* **165**, 305 (2003).
- [64] R. Gobrecht, *Phys. Status Solidi* **13**, 429 (1966).
- [65] J. Noffsinger, E. Kioupakis, C. G. Van de Walle, S. G. Louie, and M. L. Cohen, *Phys. Rev. Lett.* **108**, 167402 (2012).
- [66] N. F. Quackenbush, J. P. Allen, D. O. Scanlon, S. Sallis, J. A. Hewlett, A. S. Nandur, B. Chen, K. E. Smith, C. Weiland, D. A. Fischer, J. C. Woicik, B. E. White, G. W. Watson, and L. F. J. Piper, *Chem. Mater.* **25**, 3114 (2013).
- [67] G. Hautier, A. Miglio, D. Waroquiers, G.-M. Rignanese, and X. Gonze, *Chem. Mater.* **26**, 5447 (2014).
- [68] K. Kuhar, M. Pandey, K. S. Thygesen, and K. W. Jacobsen, *ACS Energy Lett.* **3**, 436 (2018).
- [69] J. Tate, H. L. Ju, J. C. Moon, A. Zakutayev, A. P. Richard, J. Russell, and D. H. McIntyre, *Phys. Rev. B* **80**, 165206 (2009).
- [70] Y. Ogo, H. Hiramatsu, K. Nomura, H. Yanagi, T. Kamiya, M. Hirano, and H. Hosono, *Appl. Phys. Lett.* **93**, 032113 (2008).
- [71] E. Maci a-Barber, "Thermoelectric materials: Advances and applications," (Pan Stanford, 2015).
- [72] T. Kajikawa, N. Kimura, and T. Yokoyama, in *Proceedings ICT'03. 22nd International Conference on Thermoelectrics (IEEE Cat. No.03TH8726)* (2003).
- [73] C. L. Condon, S. M. Kauzlarich, F. Gascoin, and G. J. Snyder, *J. Solid State Chem.* **179**, 2252 (2006).
- [74] J. Zhang, L. Song, A. Mamakhel, M. R. V. J orgensen, and B. B. Iversen, *Chem. Mater.* **29**, 5371 (2017).
- [75] A. Zunger, *Appl. Phys. Lett.* **83**, 57 (2003).

Supplemental Material for “Computationally-driven, high throughput identification of CaTe and Li₃Sb as promising candidates for high mobility *p*-type transparent conducting materials”

Viet-Anh Ha,¹ Guodong Yu,^{1,*} Francesco Ricci,¹ Diana Dahliah,¹ Michiel van Setten,^{1,†} Matteo Giantomassi,¹ Gian-Marco Rignanese,¹ and Geoffroy Hautier^{1,‡}

¹*Institute of Condensed Matter and Nanoscience (IMCN), Université catholique de Louvain (UCLouvain),
Chemin étoiles 8, bte L7.03.01, Louvain-la-Neuve 1348, Belgium*

(Dated: November 14, 2018)

I. COMPUTATIONAL DETAILS

All details of electron-phonon interaction computations can be found from the Refs. 1 and 2. Here, we rewrite the formulas for the scattering rate (inverse of the relaxation time) and the electron-phonon coupling strength for specific phonon mode and phonon wave-vector. The scattering rates at given temperature:

$$\frac{1}{\tau_{n\mathbf{k}}} = \frac{2\pi}{\hbar} \sum_{m\nu} \int \frac{d\mathbf{q}}{\Omega_{BZ}} |g_{nm\nu}(\mathbf{k}, \mathbf{q})|^2 \times [(1 - f_{m\mathbf{k}+\mathbf{q}} + n_{\mathbf{q}\nu})\delta(\epsilon_{n\mathbf{k}} - \hbar\omega_{\mathbf{q}\nu} - \epsilon_{m\mathbf{k}+\mathbf{q}}) + (f_{m\mathbf{k}+\mathbf{q}} + n_{\mathbf{q}\nu})\delta(\epsilon_{n\mathbf{k}} + \hbar\omega_{\mathbf{q}\nu} - \epsilon_{m\mathbf{k}+\mathbf{q}})], \quad (\text{S1})$$

where, $\tau_{n\mathbf{k}}$ is relaxation time of carriers at band n and wave-vector \mathbf{k} , Ω_{BZ} is volume of Brillouin zone (BZ), $g_{nm\nu}(\mathbf{k}, \mathbf{q})$ is the first-order electron-phonon matrix element from initial Kohn-Sham state $n\mathbf{k}$ (eigenvalue $\epsilon_{n\mathbf{k}}$) to final one $m\mathbf{k} + \mathbf{q}$ (eigenvalue $\epsilon_{m\mathbf{k}+\mathbf{q}}$) associated with a phonon mode ν and wave-vector \mathbf{q} , $f_{m\mathbf{k}+\mathbf{q}} = [\exp((\epsilon_{n\mathbf{k}+\mathbf{q}} - \epsilon_F)/k_B T) + 1]^{-1}$ is Fermi-Dirac distribution of carriers at Fermi energy ϵ_F and temperature T , $n_{\mathbf{q}\nu} = [\exp(\hbar\omega_{\mathbf{q}\nu}/k_B T) - 1]^{-1}$ is Bose-Einstein distribution of phonons with frequencies $\omega_{\mathbf{q}\nu}$ at temperature T .

The scattering rates (inverse of relaxation time) as a function of energy is computed by averaging all states as

$$\frac{1}{\tau(\epsilon)} = \frac{1}{N(\epsilon)} \sum_{n\mathbf{k}} \frac{1}{\tau_{n\mathbf{k}}} \delta(\epsilon_{n\mathbf{k}} - \epsilon), \quad (\text{S2})$$

where, $N(\epsilon) = \sum_{n\mathbf{k}} \delta(\epsilon_{n\mathbf{k}} - \epsilon)$ is density of states.

The electron-phonon coupling strength of a specific phonon mode ν and wave-vector \mathbf{q}

$$\lambda_{\mathbf{q}\nu} = \frac{1}{N(\epsilon_F)\hbar\omega_{\mathbf{q}\nu}} \sum_{nm} \int \frac{d\mathbf{k}}{\Omega_{BZ}} |g_{nm\nu}(\mathbf{k}, \mathbf{q})|^2 \delta(\epsilon_{n\mathbf{k}} - \epsilon_F) \delta(\epsilon_{m\mathbf{k}+\mathbf{q}} - \epsilon_F), \quad (\text{S3})$$

where $N(\epsilon_F)$ is density of state at Fermi level. We kept our materials intrinsic by setting the Fermi level at the mid-gap and in the very general approach of EPW, all phonon modes, both inter-band and intra-band scattering mechanisms are taken into account in the computation of scattering rates.

The hole mobilities μ_h can then be calculated as

$$\mu_h = \sigma_h / n_h e, \quad (\text{S4})$$

where σ_h , n_h and e are conductivity tensor, density of holes and elementary charge respectively. In order to calculate conductivity tensor, we solve semi-classical Boltzmann transport equation (BTE). The conductivity tensor is given by

$$\sigma_{\alpha\beta}(n, \mathbf{k}) = e^2 \tau_{n\mathbf{k}} v_\alpha(n, \mathbf{k}) v_\beta(n, \mathbf{k}), \quad (\text{S5})$$

* Present address: School of Physics and Technology (SPT), Wuhan University (WHU), Wuhan 430072, China

† Present address: IMEC, 75 Kapeldreef, B-3001 Leuven, Belgium

‡ E-mail: geoffroy.hautier@uclouvain.be

where e is elementary charge and $v_\alpha(n, \mathbf{k})$ the group velocity defined through the first-derivative of the band-energy $\epsilon_{n, \mathbf{k}}$ with respect to the wave-vector \mathbf{k}

$$v_\alpha(n, \mathbf{k}) = \frac{1}{\hbar} \frac{\partial \epsilon_{n, \mathbf{k}}}{\partial k_\alpha}. \quad (\text{S6})$$

The conductivity tensor can be expressed as a function of energy by multiplying Eq. S5 by a Dirac delta and then summing over all bands and \mathbf{k} points in the Brillouin zone as

$$\sigma_{\alpha\beta}(\epsilon) = \frac{1}{N} \sum_{n, \mathbf{k}} \sigma_{\alpha\beta}(n, \mathbf{k}) \delta(\epsilon - \epsilon_{n, \mathbf{k}}), \quad (\text{S7})$$

where N is the number of \mathbf{k} points. Finally, the conductivity tensor as a function of temperature T and Fermi level μ (electronic chemical potential) is computed through $\sigma_{\alpha\beta}(\epsilon)$ as

$$\sigma_{\alpha\beta}(T; \mu) = \frac{1}{\Omega} \int \sigma_{\alpha\beta}(\epsilon) \left[-\frac{\partial f_\mu(T; \epsilon)}{\partial \epsilon} \right] d\epsilon, \quad (\text{S8})$$

where f_μ is the Fermi-Dirac distribution and Ω is the volume of the unit cell. The Fermi level μ is defined correspondingly to a given doping carrier concentration.

Here, we used the BoltzTrap package [3] to solve BTE. In practice, BoltzTrap interpolates the DFT band-energies (computed on a finite number of \mathbf{k} -points) using star functions (see section 2 of Ref. 3). Hence, the group velocities in Eq. S6 can be easily obtained on a much denser \mathbf{k} -point grid thus facilitating the numerical convergence of the final results. In constant relaxation-time approximation, the calculations based on the interpolation of band-energies can produce many transport quantities such as conductivity, mobility, Seebeck coefficient, *etc.* as long as the relaxation-time is known. In this work, we go beyond this approximation using $\tau_{n, \mathbf{k}}$ computed by EPW. We implement an interpolation for relaxation time in BoltzTrap on the same very dense \mathbf{k} -point grid used for band-energies. The physical principle for this implementation is that the symmetries of the self-energy are the same as those of band-energies [4] ($\tau_{n, \mathbf{k}}$ can be calculated from the imaginary part of the electron self-energy in interaction with phonons).

II. RESULTS

Table SI shows information of 107 materials passing through the first two filters and then computed with HSE to obtain more accurate band gaps and direct gaps.

TABLE SI: Formula, space group (SG), Materials Project identification number [5, 6], three principal hole effective masses m_1 , m_2 and m_3 (in m_0 -free electron mass) (the data of effective masses is reported in the previous work[7]), stability measured by the energy above hull E_{hull} in the phase diagram (in meV/atom), fundamental E_g and direct gaps E_g^d (in eV) computed using PBE and HSE [8, 9].

Formula	SG	MP-id	m_1	m_2	m_3	E_{hull}	E_g		E_g^d	
							PBE	HSE	PBE	HSE
BeS	$F\bar{4}3m$	422	0.65	0.65	0.65	0.0	3.14	4.05	5.62	6.89
KMgH ₃	$Pm\bar{3}m$	23737	0.75	0.75	0.75	0.0	2.46	3.58	4.51	5.76
SiC	$F\bar{4}3m$	8062	0.58	0.58	0.58	0.7	1.39	2.25	4.53	5.75
CsPbCl ₃	$Amm2$	675524	0.30	0.32	0.33	0.0	2.46	5.69	2.41	5.69
BeSe	$F\bar{4}3m$	1541	0.55	0.55	0.55	0.0	2.69	3.36	4.22	5.27
BeCN ₂	$I\bar{4}2d$	15703	0.75	0.75	0.78	0.0	3.85	5.21	3.85	5.21
RbPbF ₃	Cc	674508	0.71	0.83	0.95	0.0	3.81	4.84	4.10	5.20
MgS	$Fm\bar{3}m$	1315	0.98	0.98	0.98	0.0	2.79	3.84	3.61	4.95
RbHgF ₃	$Pm\bar{3}m$	7482	0.93	0.93	0.93	0.0	0.65	2.11	2.70	4.90
AgCl	$Fm\bar{3}m$	22922	0.83	0.83	0.83	0.0	0.95	2.28	2.89	4.81
CsHgF ₃	$Pm\bar{3}m$	561947	0.89	0.89	0.89	0.0	0.76	2.20	2.43	4.59
Be ₂ C	$Fm\bar{3}m$	1569	0.37	0.37	0.37	0.0	1.19	1.63	4.12	4.56
SrMgH ₄	$Cmc2_1$	643009	0.84	0.90	0.95	0.0	2.74	3.78	3.27	4.52
Li ₂ Se	$Fm\bar{3}m$	2286	0.95	0.95	0.95	0.0	3.00	3.70	3.36	4.36
BP	$F\bar{4}3m$	1479	0.34	0.34	0.34	0.0	1.24	2.26	3.39	4.35
CaS	$Fm\bar{3}m$	1672	0.88	0.88	0.88	0.0	2.39	3.34	3.18	4.28
LiCa ₄ B ₃ N ₆	$Im\bar{3}m$	6799	0.86	0.86	0.86	0.0	2.21	3.38	2.98	4.25

Continued on next page

TABLE SI – continued from previous page

Formula	SG	MP-id	m_1	m_2	m_3	E_{hull}	E_g		E_g^d	
							PBE	HSE	PBE	HSE
BaSrI ₄	$R\bar{3}m$	754852	0.73	0.73	0.80	21.8	3.37	4.22	3.35	4.22
LiSr ₄ B ₃ N ₆	$Im\bar{3}m$	9723	0.89	0.89	0.89	0.0	2.09	3.22	2.95	4.18
NaSr ₄ B ₃ N ₆	$Im\bar{3}m$	10811	0.92	0.92	0.92	0.0	1.99	3.14	2.78	4.08
K ₂ LiAlH ₆	$Fm\bar{3}m$	24411	0.65	0.65	0.65	9.1	2.45	3.70	2.93	4.04
BeTe	$F\bar{4}3m$	252	0.42	0.42	0.42	0.0	2.02	2.45	3.62	4.04
Ba ₃ SrI ₈	$I4/mmm$	756235	0.70	0.81	0.81	7.5	3.23	4.02	3.23	4.02
CaSe	$Fm\bar{3}m$	1415	0.77	0.77	0.77	0.0	2.09	2.95	2.99	4.01
LiH	$Fm\bar{3}m$	23703	0.46	0.46	0.46	0.0	3.02	3.97	2.97	3.97
AlP	$F\bar{4}3m$	1550	0.56	0.56	0.56	0.0	1.63	2.50	3.09	3.90
YbS	$Fm\bar{3}m$	1820	0.76	0.76	0.76	0.0	2.22	2.96	2.91	3.76
Na ₂ LiAlH ₆	$Fm\bar{3}m$	644092	0.66	0.66	0.66	3.9	2.64	3.75	2.89	3.75
SrSe	$Fm\bar{3}m$	2758	0.83	0.83	0.83	0.0	2.23	3.03	2.80	3.68
BaLiH ₃	$Pm\bar{3}m$	23818	0.36	0.36	0.36	0.0	2.27	3.26	2.55	3.62
CsPbF ₃	$Pm\bar{3}m$	5811	0.39	0.39	0.39	4.6	3.05	3.59	2.92	3.59
Cs ₃ ZnH ₅	$I4/mcm$	643702	0.69	0.93	0.93	0.0	2.75	3.58	2.79	3.58
Al ₂ CdS ₄	$Fd\bar{3}m$	9993	0.78	0.78	0.78	20.0	2.47	3.55	2.47	3.56
K ₂ LiAlH ₆	$R\bar{3}m$	23774	0.68	0.84	0.84	0.0	2.58	3.52	2.90	3.52
BaMgH ₄	$Cmcm$	643718	0.48	0.55	0.70	4.8	2.32	3.26	2.58	3.51
CaTe	$Fm\bar{3}m$	1519	0.60	0.60	0.60	0.0	1.55	2.18	2.62	3.50
Cs ₃ MgH ₅	$P4/ncc$	23947	0.88	0.93	0.93	0.3	2.61	3.49	2.63	3.49
Cs ₃ MgH ₅	$I4/mcm$	643895	0.83	0.94	0.94	0.0	2.59	3.49	2.61	3.49
YbSe	$Fm\bar{3}m$	286	0.67	0.67	0.67	0.0	1.97	2.43	2.77	3.48
ZnS	$F\bar{4}3m$	10695	0.81	0.81	0.81	0.0	2.02	3.46	2.02	3.46
TaCu ₃ S ₄	$P\bar{4}3m$	10748	0.98	0.98	0.98	0.0	1.95	2.95	2.34	3.46
Al ₂ ZnS ₄	$Fd\bar{3}m$	4842	0.66	0.66	0.66	0.0	2.49	3.43	2.52	3.46
Li ₂ ThN ₂	$P\bar{3}m1$	27487	0.85	0.95	0.95	0.0	2.18	3.33	2.34	3.46
Mg ₂ B ₂₄ C	$P\bar{4}n2$	568556	0.77	0.93	0.93	0.0	2.63	3.41	2.62	3.42
Li ₂ GePbS ₄	$I\bar{4}2m$	19896	0.61	0.61	0.98	0.0	2.25	3.20	2.31	3.33
Cs ₃ H ₅ Pd	$P4/mbm$	643006	0.79	0.83	0.83	0.0	2.28	3.09	2.38	3.32
SrTe	$Fm\bar{3}m$	1958	0.67	0.67	0.67	0.0	1.77	2.39	2.48	3.24
MgTe	$F\bar{4}3m$	13033	0.95	0.95	0.95	0.9	2.32	3.24	2.32	3.24
CsTaN ₂	$I\bar{4}2d$	34293	0.71	0.71	0.92	0.0	2.15	3.22	2.21	3.22
Cs ₃ MnH ₅	$I4/mcm$	643706	0.82	0.96	0.96	0.0	1.65	3.18	1.66	3.21
LiMgP	$F\bar{4}3m$	36111	0.65	0.65	0.65	0.0	1.56	2.00	2.39	3.18
BaS	$Fm\bar{3}m$	1500	0.85	0.85	0.85	0.0	2.16	3.02	2.30	3.17
LiAlTe ₂	$I\bar{4}2d$	4586	0.52	0.83	0.83	0.0	2.44	3.11	2.44	3.11
YbTe	$Fm\bar{3}m$	1779	0.54	0.54	0.54	0.0	1.47	1.76	2.46	3.09
Li ₃ Sb	$Fm\bar{3}m$	2074	0.24	0.24	0.24	0.0	0.72	1.15	2.28	3.06
SrAl ₂ Te ₄	$I422$	37091	0.42	0.79	0.80	0.0	1.50	2.66	1.55	3.06
TaCu ₃ Te ₄	$P\bar{4}3m$	9295	0.63	0.63	0.63	0.0	1.14	2.50	1.59	3.05
TaCu ₃ Se ₄	$P\bar{4}3m$	4081	0.82	0.82	0.82	0.0	1.63	2.43	2.03	2.98
BaSe	$Fm\bar{3}m$	1253	0.76	0.76	0.76	0.0	1.96	2.59	2.19	2.95
KAg ₂ PS ₄	$I\bar{4}2m$	12532	0.67	0.82	0.82	0.0	1.27	2.53	2.05	2.87
AlAs	$F\bar{4}3m$	2172	0.50	0.50	0.50	0.0	1.52	2.12	1.77	2.84
LiErS ₂	$I4_1/amd$	35591	0.62	0.99	0.99	10.4	1.99	2.80	1.99	2.80
GaN	$F\bar{4}3m$	830	0.94	0.94	0.94	5.2	1.57	2.80	1.56	2.80
CsPbCl ₃	$Pm\bar{3}m$	23037	0.26	0.26	0.26	5.5	2.40	2.75	2.19	2.75
GaP	$F\bar{4}3m$	2490	0.45	0.45	0.45	0.0	1.59	1.97	1.59	2.69
LiSmS ₂	$I4_1/amd$	34477	0.93	0.93	0.99	0.0	1.92	2.69	1.92	2.69
LiGaTe ₂	$I\bar{4}2d$	5048	0.37	0.70	0.70	0.0	1.59	2.69	1.59	2.69
ThSnI ₆	$P\bar{3}1c$	28815	0.55	0.57	0.57	20.8	1.99	2.32	2.23	2.66
BaTe	$Fm\bar{3}m$	1000	0.64	0.64	0.64	0.0	1.59	2.22	1.97	2.65
CuI	$F\bar{4}3m$	22895	0.86	0.86	0.86	6.0	1.14	2.65	1.13	2.65
NbCu ₃ Se ₄	$P\bar{4}3m$	4043	0.82	0.82	0.82	0.0	1.40	2.12	1.79	2.64
TaSbRu	$F\bar{4}3m$	31454	0.73	0.73	0.73	0.0	0.71	1.30	1.84	2.63
Nd ₂ TeS ₂	$P\bar{3}m1$	10933	0.45	0.72	0.72	0.0	1.62	2.23	1.95	2.63
Zr ₂ SN ₂	$P6_3/mmc$	11583	0.40	0.54	0.54	0.0	0.56	1.38	1.62	2.62
Ca ₃ PbCl ₃	$Pm\bar{3}m$	29342	0.63	0.63	0.63	0.0	1.84	2.60	1.84	2.60

Continued on next page

TABLE SI – continued from previous page

Formula	SG	MP-id	m_1	m_2	m_3	E_{hull}	E_g		E_g^d	
							PBE	HSE	PBE	HSE
BaMg ₂ P ₂	$P\bar{3}m1$	8278	0.62	0.62	0.88	0.0	1.15	1.69	1.75	2.60
WS ₂	$R\bar{3}m$	9813	0.79	0.91	0.91	3.8	1.34	2.12	1.84	2.60
Ca ₃ AsCl ₃	$Pm\bar{3}m$	28069	0.58	0.58	0.58	0.0	1.84	2.57	1.84	2.57
BaSnS ₂	$P2_1/c$	12181	0.44	0.57	0.85	0.0	1.62	2.40	1.69	2.54
LiZnP	$F\bar{4}3m$	10182	0.40	0.40	0.40	0.0	1.36	1.69	1.50	2.51
ScCuS ₂	$P\bar{3}m1$	6980	0.75	0.75	0.87	0.0	0.88	1.77	1.50	2.50
SbIrS	$Pca2_1$	9270	0.50	0.52	0.89	4.5	1.04	1.76	1.54	2.43
Cd ₂ P ₃ Cl	Cc	29246	0.41	0.76	0.80	9.1	1.12	2.06	1.58	2.42
CsPbBr ₃	$Pnma$	567629	0.25	0.28	0.29	0.0	2.01	2.39	2.01	2.39
Hg ₂ P ₃ Cl	$C2/c$	28875	0.40	0.82	0.99	2.3	1.13	1.89	1.56	2.38
Cd ₂ P ₃ Br	$C2/c$	29245	0.44	0.78	0.87	6.8	1.05	2.01	1.57	2.37
CsNbN ₂	$Fd\bar{3}m$	8978	0.53	0.53	0.53	8.2	1.53	2.36	1.53	2.36
RbGeBr ₃	$Pna2_1$	28558	0.32	0.42	0.47	0.0	1.99	2.34	1.99	2.34
SbIrS	$P2_13$	8630	0.39	0.39	0.39	0.0	1.42	2.18	1.56	2.34
Ca ₃ AsBr ₃	$Pm\bar{3}m$	27294	0.57	0.57	0.57	0.0	1.67	2.34	1.67	2.34
LiYSe ₂	$I4_1/amd$	37879	0.55	0.83	0.83	17.6	1.55	2.33	1.55	2.33
ZrCoBi	$F\bar{4}3m$	31451	0.80	0.80	0.80	0.0	1.15	1.28	1.66	2.31
NaLi ₂ Sb	$Fm\bar{3}m$	5077	0.41	0.41	0.41	0.0	0.71	1.04	1.61	2.27
ZnP ₂	$P4_12_12$	2782	0.37	0.65	0.65	0.0	1.47	2.14	1.59	2.27
KHgF ₃	$Pm\bar{3}m$	7483	0.87	0.87	0.87	0.0	0.64	2.26	2.82	2.26
LiHoSe ₂	$I4_1/amd$	33322	0.52	0.83	0.83	16.8	1.58	2.25	1.58	2.25
LiDySe ₂	$I4_1/amd$	35717	0.55	0.81	0.82	16.0	1.56	2.23	1.56	2.23
P ₂ Pt	$Pa\bar{3}$	730	0.25	0.25	0.25	0.0	1.06	1.79	1.51	2.22
TbLiSe ₂	$I4_1/amd$	38695	0.61	0.78	0.78	15.4	1.54	2.20	1.54	2.20
MgGeP ₂	$I\bar{4}2d$	34903	0.26	0.61	0.61	13.0	1.51	2.16	1.54	2.16
LiSmSe ₂	$I4_1/amd$	35388	0.72	0.72	0.75	0.0	1.51	2.15	1.51	2.15
LiNdSe ₂	$I4_1/amd$	37605	0.72	0.72	0.84	7.6	1.52	2.15	1.52	2.15
SrMg ₂ Sb ₂	$P\bar{3}m1$	9566	0.53	0.55	0.55	0.0	0.98	1.42	1.51	2.06
RbAu	$Pm\bar{3}m$	30373	0.24	0.24	0.24	0.0	0.57	0.49	1.80	2.02
CsAu	$Pm\bar{3}m$	2667	0.25	0.25	0.25	0.0	1.02	1.25	1.73	1.99
LiNbS ₂	$P6_3/mmc$	7936	0.61	0.61	0.68	0.0	0.73	1.06	1.56	1.95
Ag ₃ SbS ₃	$R\bar{3}c$	4515	0.49	0.49	1.00	2.3	1.00	1.30	1.54	1.94

Table III shows information of current n -type TCMs. Most of them exhibits mobility at the order of 100 cm²/Vs.

TABLE III: The current n -type TCMs, fabrication methods (abbreviations of some methods are at the bottom of this table), sorts of dopants used, electron carrier concentrations C (in cm⁻³) and mobilities μ (in cm²/Vs). These values are extracted from experimental measurements (as cited references) at room-temperature. The values of mobility depend on morphologies of fabricated-samples such as single crystal, polycrystalline, amorphous, thin-film,...

n -TCMs	Processing	Dopants	C (cm ⁻³)	μ (cm ² /Vs)
SnO ₂	CVD	Sb	8.5×10^{15}	260 [10]
	CVD	Sb	8.6×10^{16}	240 [10]
	CVD	Sb	2.2×10^{18}	150 [10]
	PLD	Ta	2.7×10^{20}	83 [11]
	PLD	Sb	$\sim 1 \times 10^{19}$	~ 40 [12]
ZnO	VPT	Undoped	6×10^{16}	205 [13]
	†	†	$10^{15} - 10^{20}$	50-230 [14, 15]
	PLD	Undoped	3×10^{16}	155 [16]
	Sputtering	Al	3.6×10^{20}	41.3 [17]
	Sputtering	Al	8×10^{20}	17 [18, 19]
In ₂ O ₃	PVD	-	$3 - 9 \times 10^{17}$	160 [20]
	ST	Sn	$0.1 - 6 \times 10^{20}$	30-70 [21]
	Sputtering	Undoped	$10^{17} - 10^{20}$	< 10 [22]
	VEM	Undoped	3.5×10^{19}	25 - 60 [23]
VEM	Undoped	4.69×10^{20}	74 [24]	

Continued on next page

TABLE SII – continued from previous page

n -TCMs	Processing	Dopants	C (cm ⁻³)	μ (cm ² /Vs)	
	EBE	Sn	0.46 – 8.6 × 10 ²⁰	43 – 79 [25]	
	Flux	Sn	1.6 × 10 ²⁰	100 [26]	
	Sputtering	Sn	6 × 10 ²⁰	~ 25 [27]	
	TRE	Mo	2.5 – 3.5 × 10 ²⁰	80 – 130 [28]	
	PLD	Mo	1.9 × 10 ²⁰	95 [29]	
	Sputtering	H	1.4 – 1.8 × 10 ²⁰	98 – 130 [30]	
	Sputtering	H	1.5 × 10 ²⁰	140 [31]	
	Sputtering	Sn	1 × 10 ²¹	40 [32]	
	Ga ₂ O ₃	Verneuil	Undoped	1 × 10 ¹⁸	80 [33]
		FZM	Undoped	1.2 – 5.2 × 10 ¹⁸	2.6 – 46 [34]
EFG		Undoped	1 × 10 ¹⁷	153 [35]	
-	-	Undoped	8 × 10 ¹⁶	~ 150 [36]	
CVD: Chemical vapor deposition			PLD: Pulsed laser deposition		
VPT: Vapor phase transport			‡: Reviewed from many papers		
PVD: Physical vapor deposition			ST: Spray technique		
VEM: Vacuum evaporation method			EBE: e-beam evaporation		
TRE: Thermal reactive evaporation			FZM: Floating zone method		
EFG: Edge-defined film-fed growth					

Table SIII shows information for different A₃B compounds (A = Li, Na, K, Rb and Cs; and B = N, P, As and Sb). The very unstable compounds are not considered here. The data of compounds with narrow gap $E_g < 0.4$ eV is not presented because the values of effective masses are not reliable.

TABLE SIII: Formula, space group (SG), Materials Project identification number [5, 6], fundamental E_g computed with DFT (in eV), three principal hole effective masses m_1 , m_2 and m_3 (m_o -free electron mass) and stability measured by energy above hull E_{hull} in the phase diagram (in meV/atom).

Formula	SG	MP-id	E_g	m_1	m_2	m_3	E_{hull}
Li ₃ N	$P6/mmm$	2251	0.98	1.09	1.09	5.30	0.0
Li ₃ N	$P6_3/mmc$	2341	1.22	1.60	1.60	3.66	10.0
Li ₃ P	$P6_3/mmc$	736	0.70	0.84	0.84	2.41	0.0
Li ₃ As	$P6_3/mmc$	757	0.64	0.74	0.74	2.10	0.0
Li ₃ Sb	$P6_3/mmc$	7955	0.48	0.61	0.61	1.75	3.0
Li ₃ Sb	$Fm\bar{3}m$	2074	0.85	0.24	0.24	0.24	0.0
Na ₃ P	$P6_3/mmc$	1598	0.41	1.61	1.61	6.52	0.0
Na ₃ Sb	$P6_3/mmc$	7956	0.40	1.10	1.10	3.85	0.0
K ₃ Sb	$Fm\bar{3}m$	10159	0.68	5.22	5.22	5.22	29.0
Rb ₃ Sb	$Fm\bar{3}m$	33018	0.43	1.71	1.71	1.71	34.0
Cs ₃ Sb	$Fm\bar{3}m$	10378	0.61	1.03	1.03	1.03	0.0

Fig. S1 presents scattering rate of both CaTe and Li₃Sb as a functions of energy at room temperature (valence band maximums (VBM) are set to zeros). The specific contributions of acoustic (the first three modes) and optical (the remaining ones) phonon-modes are also shown. We can see that the optical modes are the main source of scattering in both cases.

Fig. S2 shows electron-phonon coupling strength (see Eq. S3) for six phonon modes of CaTe computed with a dense \mathbf{q} -point mesh of $40 \times 40 \times 40$. The Fermi energy in Eq. S3 was set to 146 meV below the VBM in order to assure this quantity to be defined ($N(\epsilon_F) > 0$). Moreover, the Fermi level corresponding to very high doping of 10^{21} cm⁻³ lies 264.5 meV below the VBM so the value of 146 meV can give us the picture in the considering range of hole concentrations. The electron-phonon coupling strength $\lambda_{q\nu}$, therefore, can depict the intensity of interactions between hole carriers (around VBM) and each phonon mode. The average values of $\lambda_{q\nu}$ over all \mathbf{q} -points (shown as red lines) point out that the hole carriers interacts with optical modes (mainly mode-6) around 5 times stronger than with acoustic modes.

In the same way, Fig. S3 presents electron-phonon coupling strength for twelve phonon modes of Li₃Sb computed with a dense \mathbf{q} -point mesh of $40 \times 40 \times 40$. The Fermi energy in Eq. S3 was set to 100 meV below the VBM (the

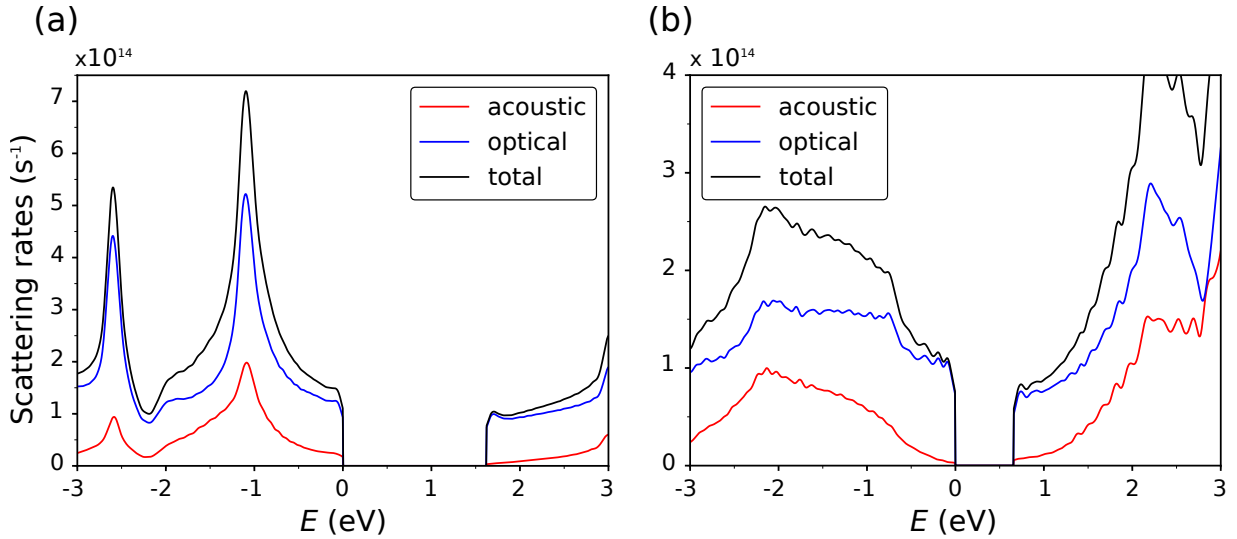


FIG. S1. Scattering rates of (a) CaTe and (b) Li_3Sb at temperature of 300 K. The contributions of acoustic and optical phonon-modes are shown as well.

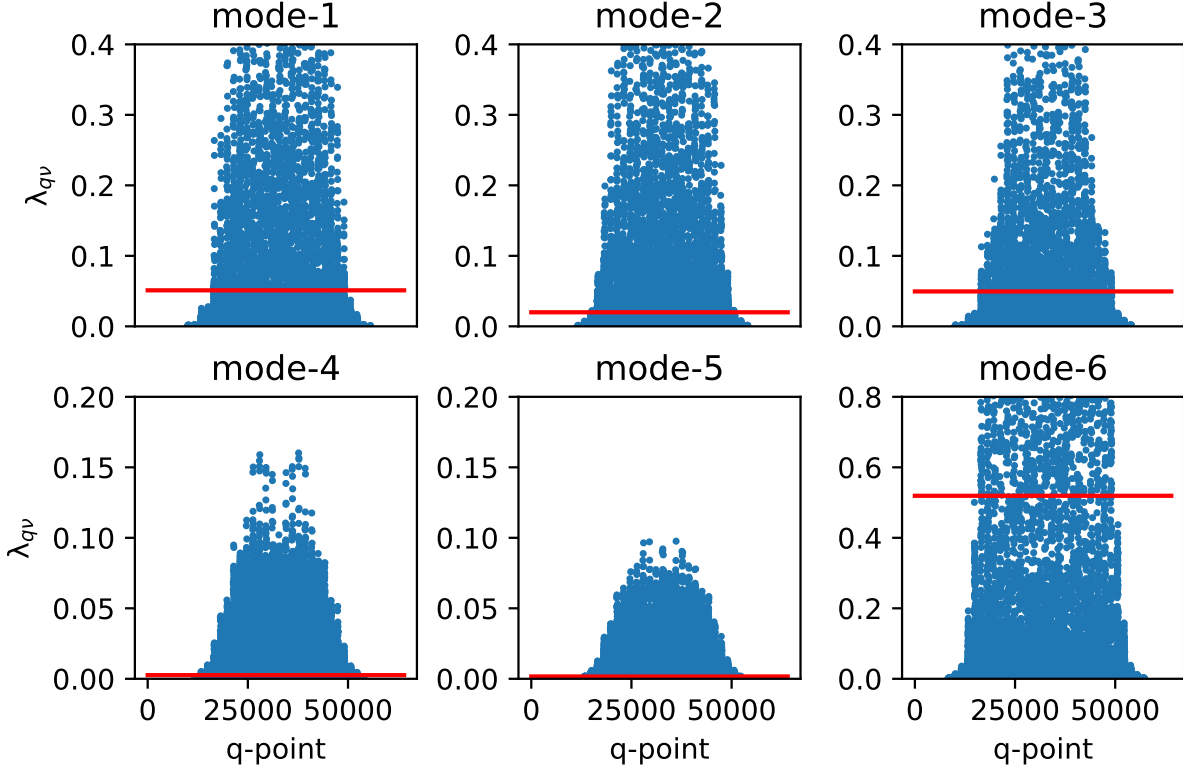


FIG. S2. The electron-phonon coupling strength of CaTe for specific mode ν and phonon wave-vector q . There are 6 phonon modes including 3 acoustic (1-3) and 3 optical ones (4-6). The number of q -points are 64000 corresponding to $40 \times 40 \times 40$ mesh in the full Brillouin zone. To reduce size of the figure, q -points with $\lambda_{\nu q} < 1 \times 10^{-3}$ are not shown in the subfigures. The red lines are average values of $\lambda_{\nu q}$ over 64000 q -points.

Fermi level at doping of 10^{21} cm^{-3} is 168.5 meV lower than VBM). In this case, the intensity of interactions (between hole carriers and phonons) with optical modes is about 19 times stronger than with acoustic modes.

We performed convergence tests for G_0W_0 calculations over the number of bands (N_b) and the kinetic energy cut-off for dielectric tensor (E_c). These two parameters will be simultaneously investigated in specific ranges, then we can choose appropriate values those give acceptable convergence of band gap. Fig. S4 and Table SIV show how band gap

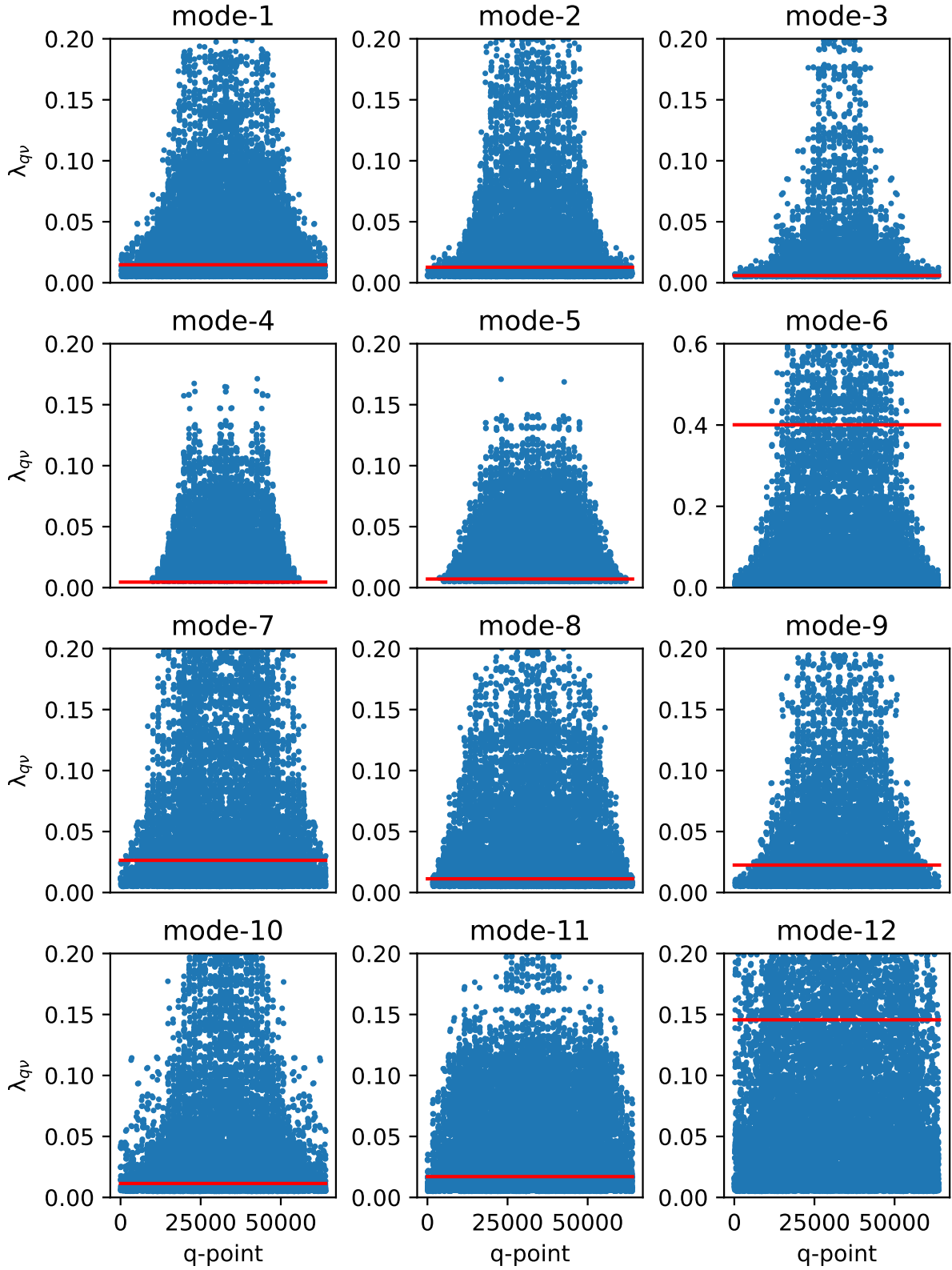


FIG. S3. The electron-phonon coupling strength of Li_3Sb for specific mode ν and phonon wave-vector q . There are 12 phonon modes including 3 acoustic (1-3) and 9 optical ones (4-12). The number of q -points are 64000 corresponding to $40 \times 40 \times 40$ mesh in the full Brillouin zone. To reduce size of the figure, q -points with $\lambda_{\nu q} < 0.5 \times 10^{-2}$ are not shown in the subfigures. The red lines are average values of $\lambda_{\nu q}$ over 64000 q -points.

at Γ point of CaTe evolves with the change of N_b and E_c . Here, $N_b = [75, 150, 300, 450]$ and $E_c = [6, 8, 10, 12, 14]$ Ha. In the same way, Fig. S5 and Table SV present how band gap at Γ point of Li_3Sb converges with the change of number of band and energy cut-off for the dielectric tensor. In the case, $N_b = [80, 160, 240, 320]$ and $E_c = [4, 6, 8, 10, 12]$ Ha. In both cases, energy cut-off for kinetic energy is set to 46 Ha and \mathbf{k} -point mesh is $6 \times 6 \times 6$.

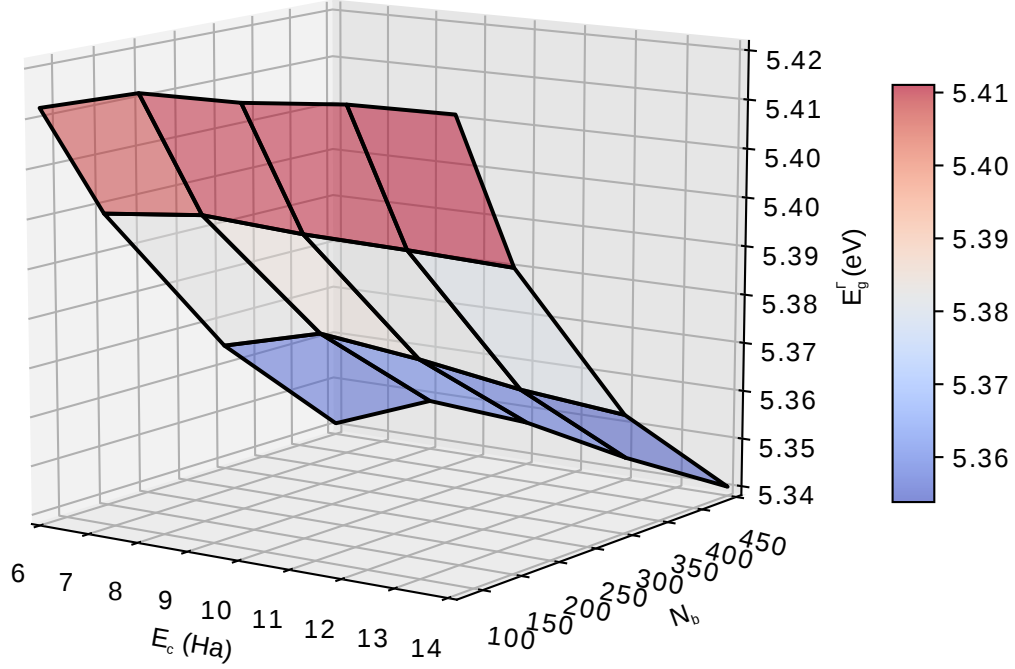


FIG. S4. The convergence test for the gap at Γ point of CaTe in G_0W_0 computation.

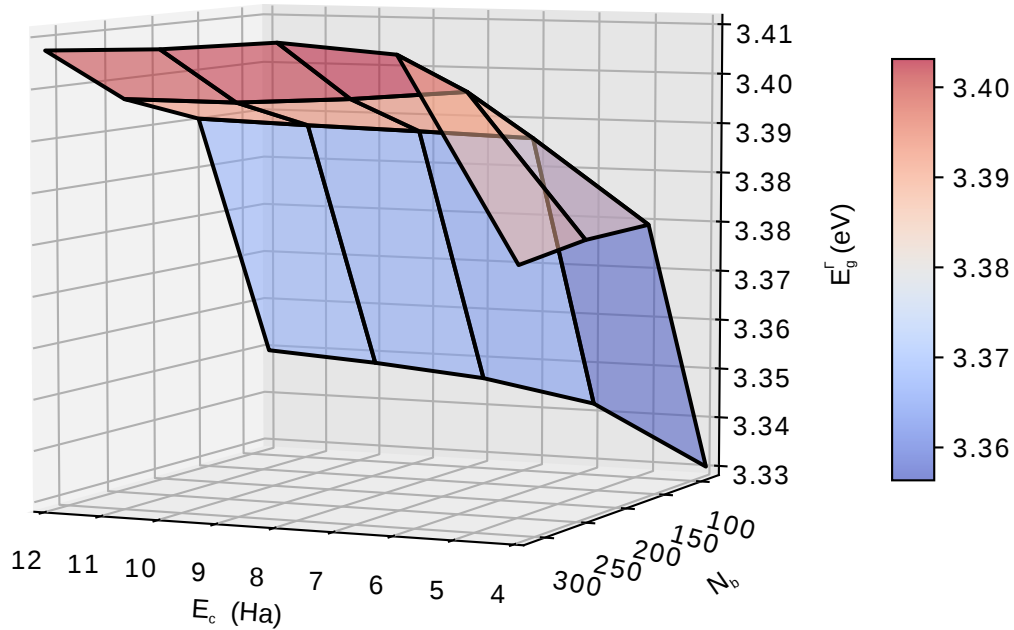


FIG. S5. The convergence test for the gap at Γ point of Li_3Sb in G_0W_0 computation.

In comparison, Fig. S6 and Fig. S7 show band structures of CaTe and Li_3Sb computed by both G_0W_0 (red) and DFT (blue).

Fig. S10, Fig. S11, Fig. S12, Fig. S13 and Fig. S14 show defect formation energies and phase diagrams of AIP, LiH, BaLiH_3 , CsH, SrTe and Al_2ZnS_4 (computed by DFT), correspondingly. The facets of phase diagrams in which

TABLE SIV. The evolution of the gap at Γ point of CaTe E_g^Γ (in eV) with the change of number of bands N_b and kinetic energy cut-off for dielectric tensor E_c (in Ha).

N_b	75	75	75	75	75	150	150	150	150	150
E_c	6.0	8.0	10.0	12.0	14.0	6.0	8.0	10.0	12.0	14.0
E_g^Γ	5.41558	5.42030	5.42063	5.42239	5.42275	5.39362	5.39570	5.39460	5.39418	5.39352
N_b	300	300	300	300	300	450	450	450	450	450
E_c	6.0	8.0	10.0	12.0	14.0	6.0	8.0	10.0	12.0	14.0
E_g^Γ	5.36266	5.36771	5.36552	5.36260	5.36077	5.34078	5.34818	5.34680	5.34287	5.34034

TABLE SV. The evolution of the gap at Γ point of Li_3Sb E_g^Γ (in eV) with the change of number of bands N_b and kinetic energy cut-off for dielectric tensor E_c (in Ha).

N_b	80	80	80	80	80	160	160	160	160	160
E_c	4.0	6.0	8.0	10.0	12.0	4.0	6.0	8.0	10.0	12.0
E_g^Γ	3.33445	3.34410	3.34744	3.34911	3.35034	3.37762	3.39112	3.39166	3.39208	3.39262
N_b	240	240	240	240	240	320	320	320	320	320
E_c	4.0	6.0	8.0	10.0	12.0	4.0	6.0	8.0	10.0	12.0
E_g^Γ	3.37743	3.40028	3.39860	3.39749	3.39752	3.37587	3.40757	3.40897	3.40748	3.40683

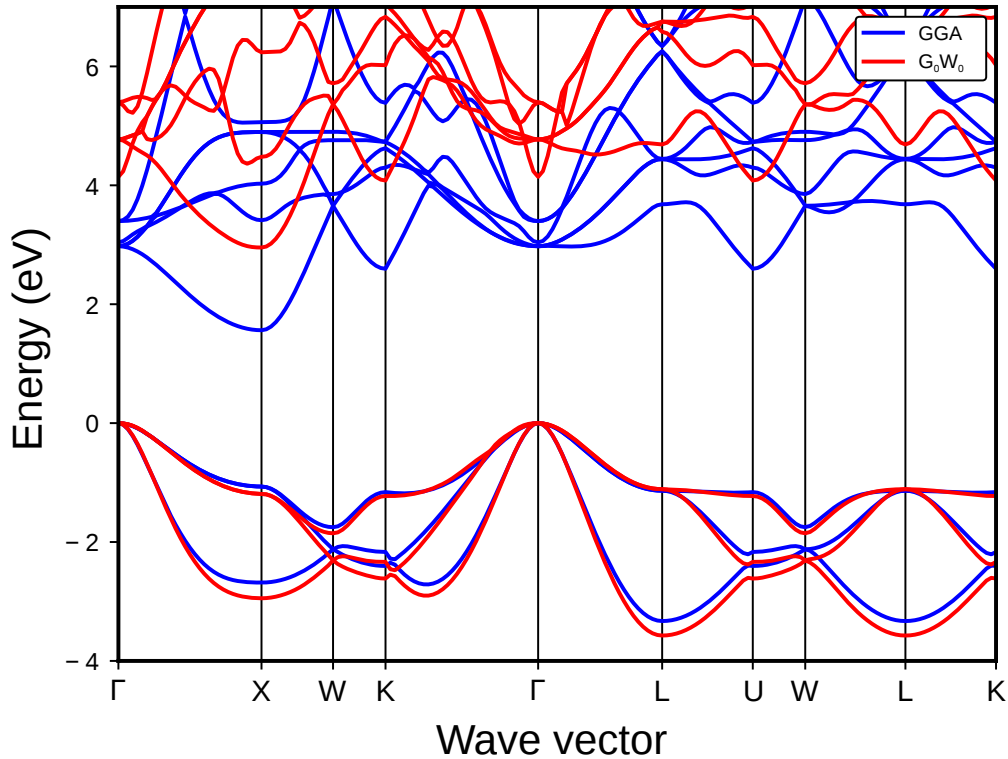


FIG. S6. The band structure of CaTe computed by DFT (blue) and G_0W_0 (red).

the chemical potentials of elements were estimated are marked to corresponding defect formation energies. It worth noting that although DFT calculations using GGA underestimate band gap, the defect formation energy computed with it is still reliable[37]. In HSE computations, the VBM shifts down while the CBM shifts up, therefore, the general

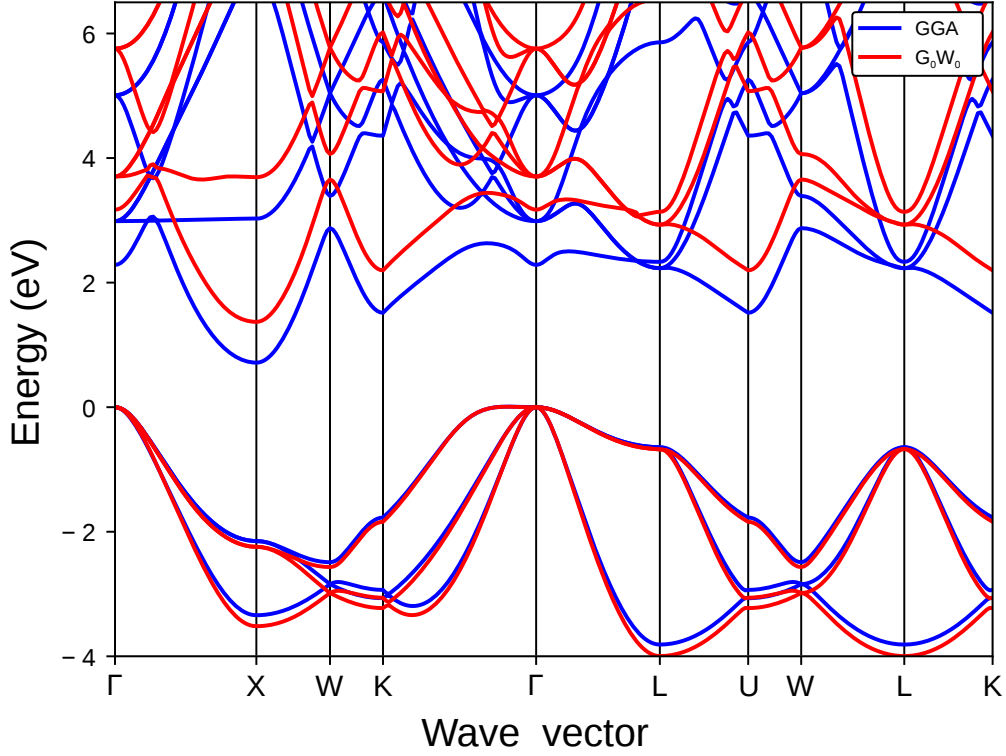


FIG. S7. The band structure of Li_3Sb computed by DFT (blue) and G_0W_0 (red).

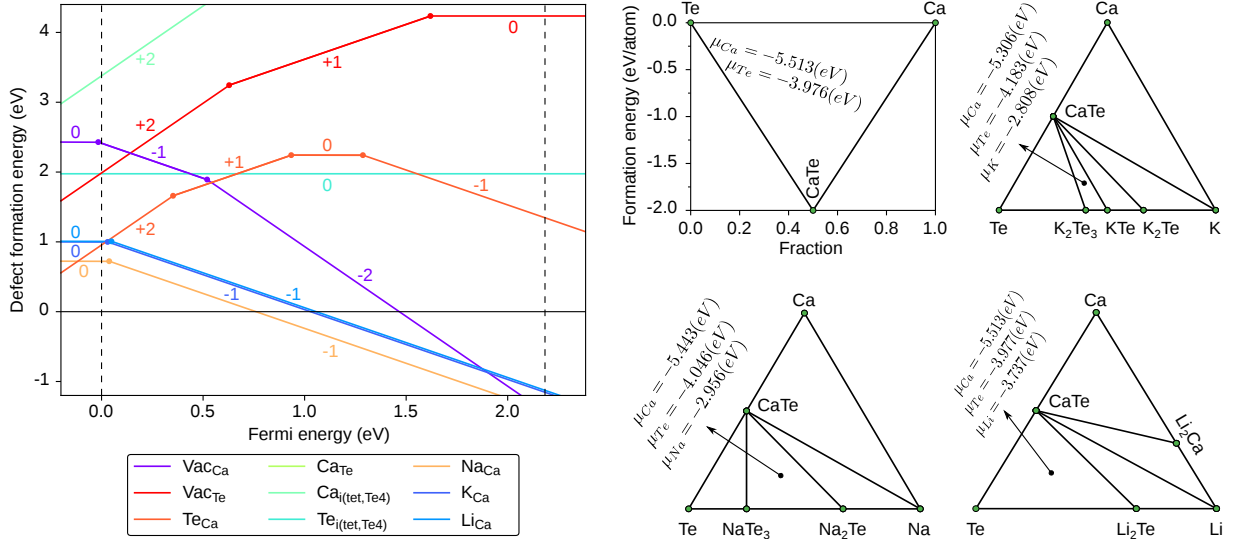


FIG. S8. The defect formation energy as a function of Fermi level of intrinsic and extrinsic defects for CaTe (left) and the phase diagrams with chemical potentials of each element in specific facets (right). The intrinsic defects include vacancies (Vac_{Ca} and Vac_{Te}), anti-sites (Te_{Ca} and Ca_{Te}) and interstitial atoms inserting into the tetrahedral hollows formed by 4 Te atoms ($\text{Ca}_{i(\text{tet,Te4})}$ and $\text{Te}_{i(\text{tet,Te4})}$) while Na, K and Li are used as the extrinsic defects substituting onto Ca-sites (Na_{Ca} , K_{Ca} and Li_{Ca}). The chemical potential of elements are obtained from phase diagrams of Ca-Te and Ca-Te-X ($X=\text{Na}$, K and Li) for intrinsic and extrinsic defects, respectively. The VBM is set to zero.

trend of defect formation energy is similar to that in DFT-GGA computations. The change of formation energy is small as well[37].

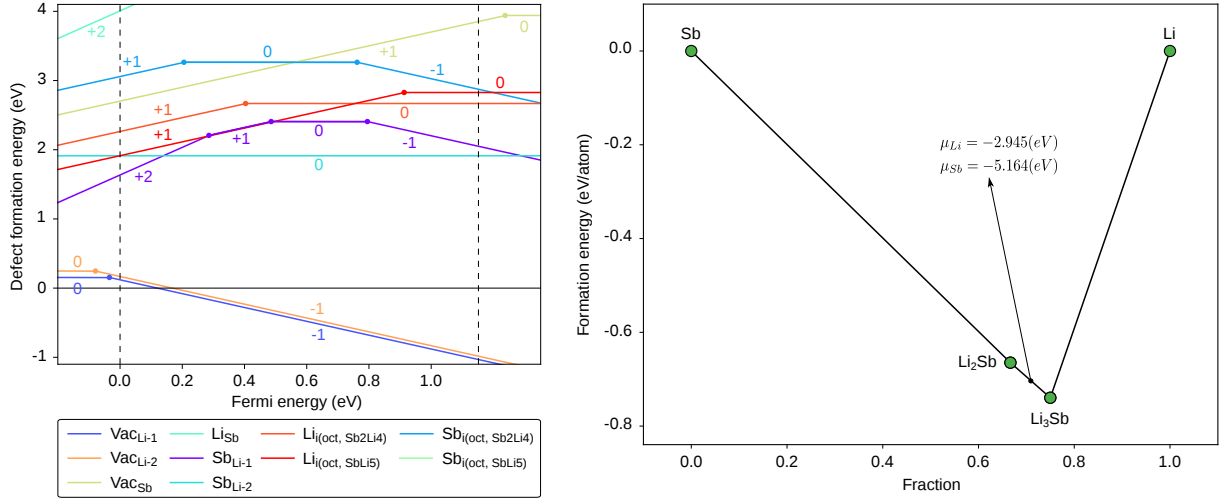


FIG. S9. The defect formation energy as a function of Fermi level of intrinsic defects for Li_3Sb (left) and the phase diagram with chemical potentials of each element in a specific facet (right). The intrinsic defects include vacancies ($\text{Vac}_{\text{Li}-1}$, $\text{Vac}_{\text{Li}-2}$ and Vac_{Sb}), anti-sites (Li_{Sb} , $\text{Sb}_{\text{Li}-1}$ and $\text{Sb}_{\text{Li}-2}$) and interstitial atoms inserting into the octahedron hallows formed by Sb and Li atoms ($\text{Li}_{\text{i(oct, Sb2Li4)}}$, $\text{Li}_{\text{i(oct, SbLi5)}}$, $\text{Sb}_{\text{i(oct, Sb2Li4)}}$ and $\text{Sb}_{\text{i(oct, SbLi5)}}$). The chemical potentials of Li and Sb are obtained from their phase diagram. The VBM is set to zero.

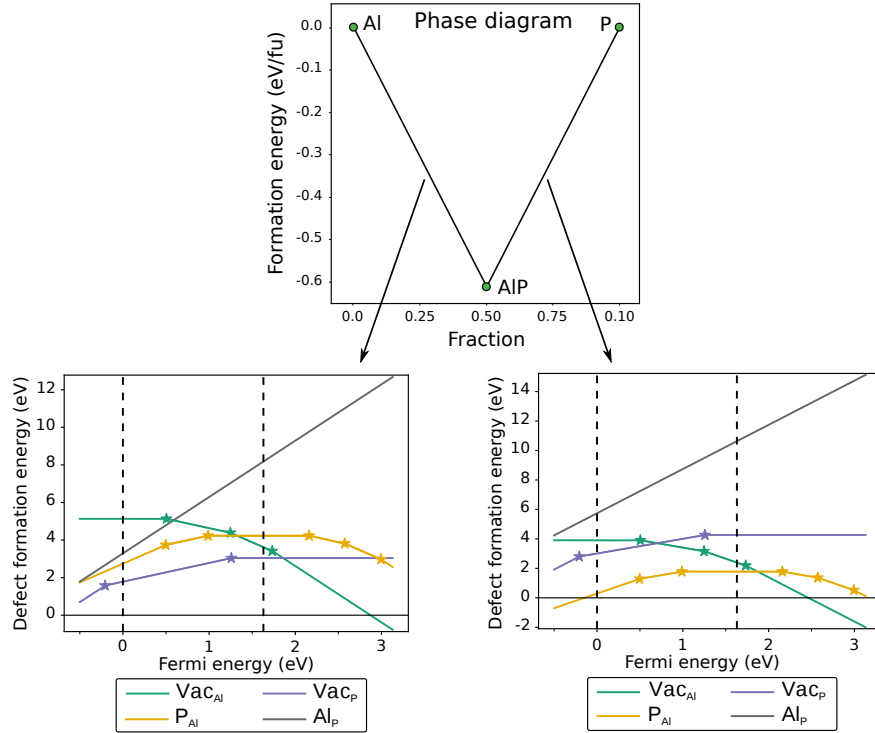


FIG. S10. The phase diagram and defect formation energies of AIP in Al-rich and P-rich conditions.

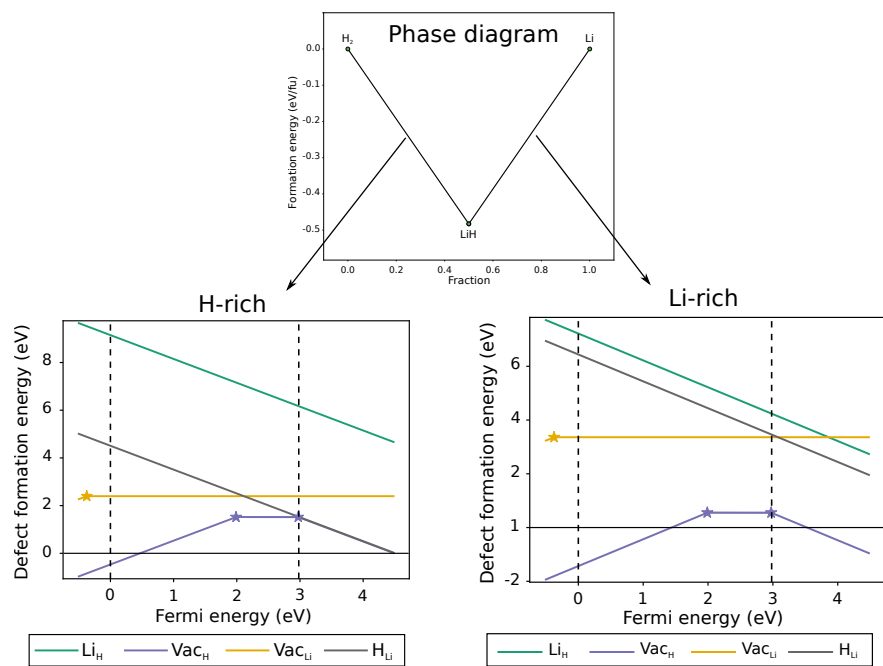


FIG. S11. The phase diagram and defect formation energies of LiH in H-rich and Li-rich conditions.

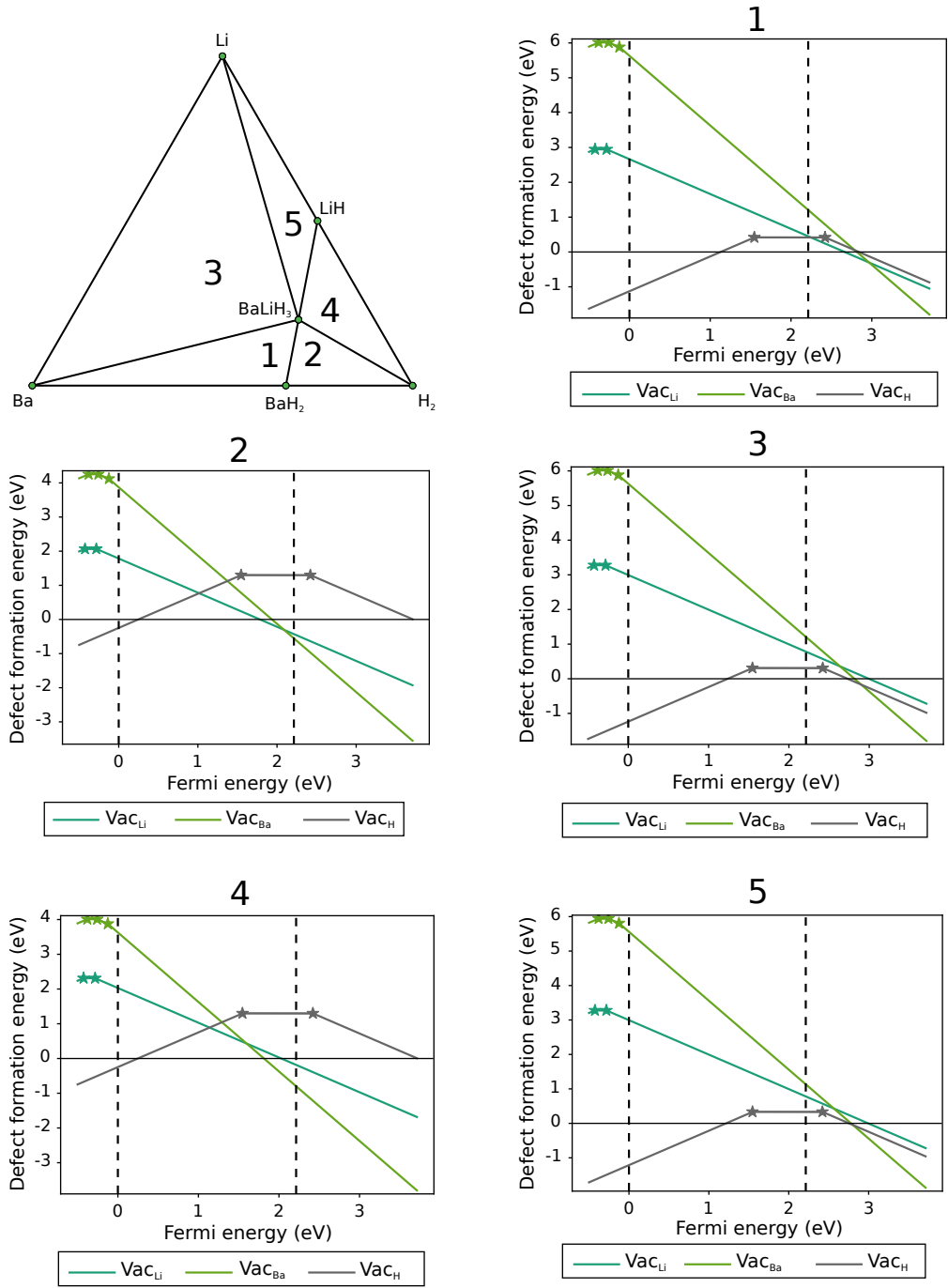


FIG. S12. The phase diagram and defect formation energies of BaLiH₃ in different conditions corresponding to the numbers marked in different facets.

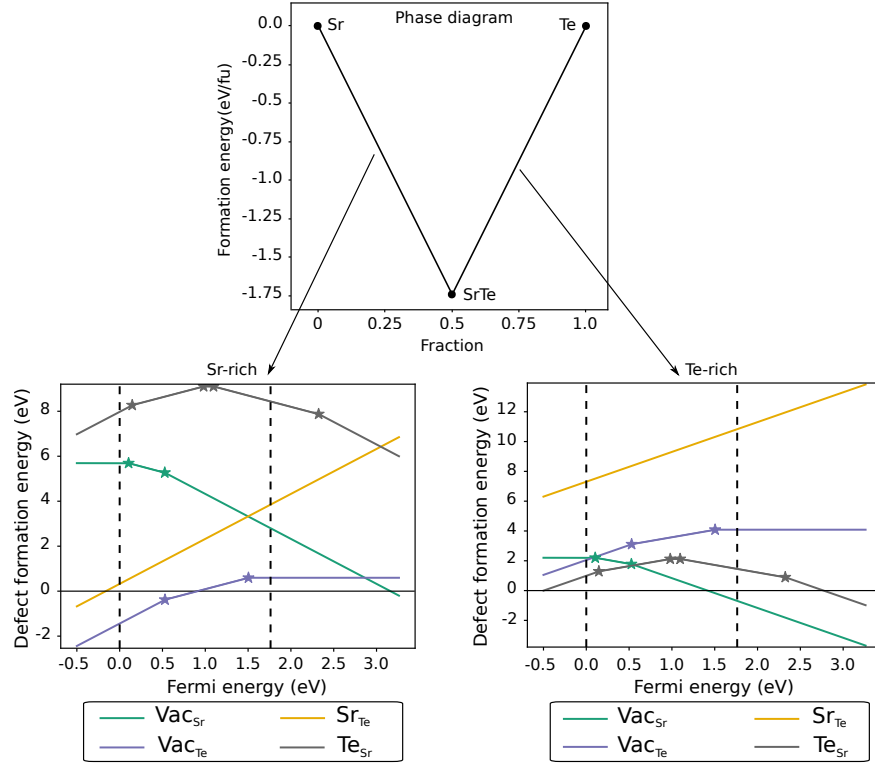


FIG. S13. The phase diagram and defect formation energies of SrTe in Sr-rich and Te-rich conditions.

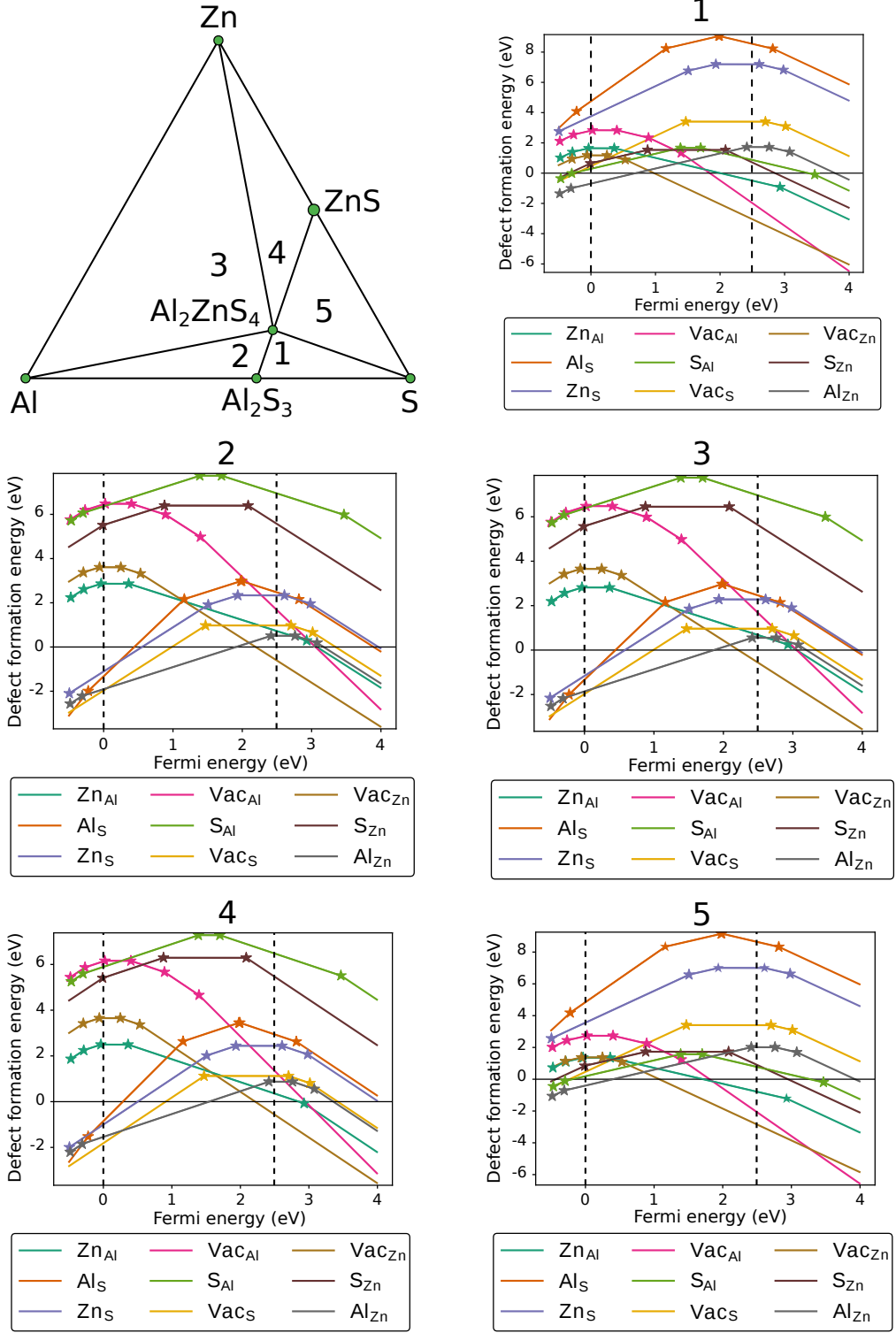


FIG. S14. The phase diagram and defect formation energies of Al_2ZnS_4 in different conditions corresponding to the numbers marked in different facets.

-
- [1] S. Poncé, E. R. Margine, C. Verdi, and F. Giustino, *Comput. Phys. Commun.* **209**, 116 (2016).
 - [2] F. Giustino, *Rev. Mod. Phys.* **89**, 015003 (2017).
 - [3] G. K. H. Madsen and D. J. Singh, *Comput. Phys. Commun.* **175**, 67 (2006).
 - [4] M. Giantomassi, *Core-electrons and self-consistency in the GW approximation from a PAW perspective*, Ph.D. thesis, Université catholique de Louvain (2009), chapter 5 and appendix B.
 - [5] A. Jain, S. P. Ong, G. Hautier, W. Chen, W. D. Richards, S. Dacek, S. Cholia, D. Gunter, D. Skinner, G. Ceder, and K. A. Persson, *APL Materials* **1**, 011002 (2013).
 - [6] “The Materials Project,” <https://www.materialsproject.org/> (2013), [accessed September 1, 2013].
 - [7] F. Ricci, W. Chen, U. Aydemir, G. J. rey Snyder, G.-M. Rignanese, A. Jain, and G. Hautier, *Sci. Data* **4**, 170085 (2017).
 - [8] J. Heyd, G. E. Scuseria, and M. Ernzerhof, *J. Chem. Phys.* **118**, 8207 (2003).
 - [9] E. N. Brothers, A. F. Izmaylov, J. O. Normand, V. Barone, and G. E. Scuseria, *J. Chem. Phys.* **129**, 011102 (2008).
 - [10] C. G. Fonstad and R. H. Rediker, *J. Appl. Phys.* **42**, 2911 (1971).
 - [11] S. Nakao, N. Yamada, T. Hitosugi, Y. Hirose, T. Shimada, and T. Hasegawa, *Appl. Phys. Express* **3**, 031102 (2010).
 - [12] J. E. Dominguez, L. Fu, and X. Q. Pan, *Appl. Phys. Lett.* **81**, 5168 (2002).
 - [13] D. C. Look, D. C. Reynolds, J. R. Sizelove, R. L. Jones, C. W. Litton, G. Cantwell, and W. C. Harsch, *Solid State Commun.* **105**, 399 (1998).
 - [14] K. Ellmer, *Nature Photon.* **6**, 809 (2012).
 - [15] D. S. Ginley, H. Hosono, and D. C. Paine, eds., “Handbook of transparent conductors,” (Springer, 2010).
 - [16] E. M. Kaidashev, M. Lorenz, H. von Wenckstern, A. Rahm, H.-C. Semmelhack, K.-H. Han, G. Benndorf, C. Bundesmann, H. Hochmuth, and M. Grundmann, *Appl. Phys. Lett.* **82**, 3901 (2003).
 - [17] C. Agashe, O. Kluth, J. Hüpkens, U. Zastrow, B. Rech, and M. Wuttig, *J. Appl. Phys.* **95**, 1911 (2004).
 - [18] K. Ellmer, F. Kudella, R. Mientus, R. Schieck, and S. Fiechter, *Semicond. Sci. Technol.* **247**, 15 (1994).
 - [19] K. Ellmer, *J. Phys. D: Appl. Phys.* **33**, 17 (2000).
 - [20] R. L. Weiher, *J. Appl. Phys.* **33**, 2834 (1962).
 - [21] R. Groth, *Phys. stat. sol.* **14**, 69 (1966).
 - [22] H. K. Müller, *Phys. Status Solidi* **27**, 723 (1968).
 - [23] S. Noguchi and H. Sakata, *J. Phys. D : Appl. Phys.* **13**, 1129 (1980).
 - [24] C. A. Pan and T. P. Ma, *J. Electron. Mater.* **10**, 43 (1981).
 - [25] I. Hamberg and C. G. Granqvist, *J. Appl. Phys.* **60**, 123 (1986).
 - [26] S. J. Wen, G. Couturier, J. P. Chaminade, E. Marquestaut, J. Claverie, and P. Hagenmuller, *J. Solid State Chem.* **101**, 203 (1992).
 - [27] M. Sawada and M. Higuchi, *Thin Solid Films* **317**, 157 (1998).
 - [28] Y. Meng, X.-L. Yang, H.-X. Chen, J. Shen, Y.-M. Jiang, Z.-J. Zhang, and Z.-Y. Hua, *Thin Solid Films* **394**, 219 (2001).
 - [29] C. Warmsingh, Y. Yoshida, D. W. Readey, C. W. Teplin, J. D. Perkins, P. A. Parilla, L. M. Gedvilas, B. M. Keyes, and D. S. Ginley, *J. Appl. Phys.* **95**, 3831 (2004).
 - [30] T. Koida, H. Fujiwara, and M. Kondo, *Jpn. J. Appl. Phys.* **46**, 685 (2007).
 - [31] T. Koida, H. Fujiwara, and M. Kondo, *Sol. Energy Mater Sol. Cells* **93**, 851 (2009).
 - [32] N. Oka, Y. Kawase, and Y. Shigesato, *Thin Solid Films* **520**, 4101 (2012).
 - [33] M. R. Lorenz and J. F. W. R. J. Gambino, *J. Phys. Chem. Solids* **28**, 403 (1967).
 - [34] N. Ueda, H. Hosono, R. Waseda, and H. Kawazoe, *Appl. Phys. Lett.* **71**, 933 (1997).
 - [35] T. Oishi, Y. Koga, K. Harada, and M. Kasu, *Appl. Phys. Express* **8**, 031101 (2015).
 - [36] N. Ma, N. Tanen, A. Verma, Z. Guo, T. Luo, H. Xing, and D. Jena, *Appl. Phys. Lett.* **109**, 212101 (2016).
 - [37] H. Peng, D. O. Scanlon, V. Stevanovic, J. Vidal, G. W. Watson, and S. Lany, *Phys. Rev. B* **88**, 115201 (2013).